


Diffusion kurtosis imaging detects the time-dependent progress of pathological changes in the oral rotenone mouse model of Parkinson's disease

Amit Khairnar^{1,2}  | Jana Ruda-Kucerova³  | Anas Arab³ | Constantinos Hadjistyllis⁵ | Albeta Sejnoha Minsterova^{1,6} | Qi Shang⁵ | Alexandra Chovsepian⁴ | Eva Drazanova^{3,7}  | Nikoletta Szabó^{8,9} | Zenon Starcuk Jr.⁷ | Irena Rektorova¹  | Francisco Pan-Montojo^{4,5}

¹Applied Neuroscience Research Group, CEITEC - Central European Institute of Technology, Masaryk University, Brno, Czech Republic

²Department of Pharmacology and Toxicology, National Institute of Pharmaceutical Education and Research (NIPER), Ahmedabad, Gandhinagar, India

³Department of Pharmacology, Faculty of Medicine, Masaryk University, Brno, Czech Republic

⁴Department of Psychiatry and Psychotherapy, University Hospital, LMU Munich, Munich, Germany

⁵Department of Neurology, University Hospital, LMU Munich, Munich, Germany

⁶Faculty of Medicine, Masaryk University, Brno, Czech Republic

⁷Institute of Scientific Instruments of the Czech Academy of Sciences, Brno, Czech Republic

⁸Department of Neurology, Faculty of Medicine, Albert Szent-Györgyi Clinical Centre, University of Szeged, Szeged, Hungary

⁹Multi-modal and Functional Neuroimaging Group, CEITEC - Central European Institute of Technology, Masaryk University, Brno, Czech Republic

Correspondence

Irena Rektorova, Applied Neuroscience Research Group, CEITEC - Central European Institute of Technology, Masaryk University, Brno, Czech Republic.
Email: irena.rektorova@fnusa.cz, irena.rektorova@ceitec.muni.cz

Funding information

This study was financed from the SoMoPro II program. The research leading to this invention acquired a financial grant from the People Programme (Marie Curie action) of the Seventh Framework Programme of the EU according to the REA Grant Agreement No. 291782. The research is further co-financed by the South-Moravian Region. The study reflects only the authors' views and the Union is not liable for any use that may be made of the information contained therein. Further co-financing was acquired within the CEITEC 2020 (LQ1601) project

Abstract

Clinical diagnosis of Parkinson's disease (PD) occurs typically when a substantial proportion of dopaminergic neurons in the substantia nigra (SN) already died, and the first motor symptoms appear. Therefore, tools enabling the early diagnosis of PD are essential to identify early-stage PD patients in which neuroprotective treatments could have a significant impact. Here, we test the utility and sensitivity of the diffusion kurtosis imaging (DKI) in detecting progressive microstructural changes in several brain regions of mice exposed to chronic intragastric administration of rotenone, a mouse model that mimics the spatiotemporal progression of PD-like pathology from the ENS to the SN as described by Braak's staging. Our results show that DKI, especially kurtosis, can detect the progression of pathology-associated changes throughout the CNS. Increases in mean kurtosis were first observed in the dorsal motor nucleus of the vagus (DMV) after 2 months of exposure to rotenone and before the loss of dopaminergic neurons in the SN occurred. Remarkably, we also show that

Abbreviations: AD, axial diffusivity; AK, axial kurtosis; ANOVA, analysis of variance; BET, brain extraction; CBW, challenging beam traversal test; CNS, central nervous system; CSF, cerebrospinal fluid; CT, computed tomography; DKI, diffusion kurtosis imaging; DMV, dorsal motor nucleus of vagus; DTI, diffusion tensor imaging; FA, fractional anisotropy; FLASH, fast low-angle shot; FOV, field of view; FSL, FMRIB software library; GFAP, glial fibrillary acidic protein; GRAPPA, generalized autocalibrating partially parallel acquisitions; HC, healthy age matched control; IC, internal capsule; MCI, mild cognitive impairment; MD, mean diffusivity; MHC II, major histocompatibility complex II; MK, mean kurtosis; MRI, magnetic resonance imaging; OF, open field; PD, Parkinson's disease; PET, positron emission tomography; RARE, rapid acquisition with relaxation enhancement; RBW, round beam walk test; RD, radial diffusivity; RESTORE, robust estimation of tensors by outlier rejection; RK, radial kurtosis; ROI, region of interest; ROT, rotenone; RT-QuIC, real-time quaking-induced conversion; SBW, square beam walk test; SE-EPI, spin-echo echo-planar imaging; SN, substantia nigra; TBSS, tract-based spatial statistics; TH, tyrosine hydroxylase; TR, repetition time; VEH, vehicle; α -Syn, alpha synuclein.

Amit Khairnar and Jana Ruda-Kucerova contributed equally for the first authorship. Irena Rektorova and Francisco Pan-Montojo contributed equally for the last authorship.

with financial contributions from the Ministry of Education, Youth and Sports of the Czech Republic, within special support paid from the National Programme For Sustainability II Funds. Further co-financing was received from project "Pharmacological research in the field of pharmacokinetics, neuropsychopharmacology, and oncology" number MUNI/A/1249/2020, with the support of the Specific University Research Grant, as provided by the Ministry of Education, Youth and Sports of the Czech Republic (MEYS CR) in the year 2021. This work performed in Munich was supported by the Deutsche Forschungsgemeinschaft (German Research Foundation) within the framework of the Munich Cluster for Systems Neurology (EXC 1010 SyNergy) and by the grant number NU20-04-00294 of the Czech Agency of Health Research. The MR measurements were supported by the grants LM2015062 and CZ.02.1.01/0.0/0.0/16_013/0001775 "National Infrastructure for Biological and Medical Imaging (Czech-BioImaging)".

limited exposure to rotenone for 2 months is enough to trigger the progression of the disease in the absence of the environmental toxin, thus suggesting that once the first pathological changes in one region appear, they can self-perpetuate and progress within the CNS. Overall, our results show that DKI can be a useful radiological marker for the early detection and monitoring of PD pathology progression in patients with the potential to improve the clinical diagnosis and the development of neuroprotective treatments.

KEYWORDS

alpha synuclein, diffusion kurtosis imaging, MRI, Parkinson, rotenone, s disease, tract-based spatial statistics

1 | INTRODUCTION

Parkinson's disease (PD) is a progressive neurodegenerative disorder affecting more than 10 million people globally (Saeed et al., 2017). PD is a heterogeneous disease featuring a number of pathological hallmarks such as degeneration of neuromelanin containing dopaminergic neurons and the presence of Lewy body pathology consisting mainly of alpha synuclein (α -Syn) (Segura-Aguilar et al., 2014). Despite a lot of ongoing research, the exact etiology of idiopathic PD remains unclear. Current treatment options for PD are symptomatic, and there is an urgent need to develop innovative disease-modifying (e.g., neuroprotective) therapies, which can slow down or halt the progression of PD pathology. Despite numerous efforts to develop such pharmacologic agents, most of these candidate drugs, which seemed to be effective in animal models, failed to show clinical efficacy (Kalia et al., 2015; Khairnar et al., 2016; Oertel, 2017). This failure might be explained by administering the new drugs to patients suffering PD in the late stage, when these agents may not be able to affect the development of pathological process anymore. It has been shown that the pathological process in PD manifested by prodromal non-motor symptoms such as rapid eye movement sleep disorders, hyposmia, and gastrointestinal dysfunction develops decades before the development of motor symptoms (Braak et al., 2003; Pan-Montojo et al., 2010; Rey et al., 2013). Since non-motor symptoms appear much earlier than motor symptoms, there is a wide time window to find subjects at the prodromal stage of the disease who are likely to develop motor symptoms of PD in the future (Heinzel et al., 2019). Therefore, there is an urgent need to develop a non-invasive biomarker, which can diagnose PD in patients presenting these prodromal symptoms. This should also allow for neuroprotective treatments to have a better outcome. Neuroimaging methods might become a suitable tool to address this unmet medical need.

The early diagnosis of PD is challenging, as there is no conclusive blood test. Recently a novel real-time quaking-induced conversion assay was developed to detect α -syn aggregates in CSF and can differentiate alpha synucleopathies from other forms of parkinsonism (van Rumund et al., 2019). However, the collection of CSF is invasive. Still, there is a lack of non-invasive biomarkers that might detect spatial patterns of α -syn seeding and neurodegeneration with the disease progression. Neurologists generally diagnose PD patients based on clinical scoring of their motor symptoms (Postuma et al., 2015). Neuroimaging methods might become a suitable tool to address this unmet medical need. Several imaging approaches have potential as sensitive and specific markers of prodromal PD, including some positron emission tomography (PET) ligands such as ^{11}C -donepezil PET/CT (cholinergic gut innervation), ^{123}I -metaiodobenzylguanidine scintigraphy (cardiac sympathetic denervation), ^{11}C -methylreboxetine PET (noradrenergic nerve terminals), or specific magnetic resonance imaging (MRI) sequences depicting brain iron (susceptibility-weighted MRI, quantitative susceptibility mapping) or neuromelanin (neuromelanin-sensitive MRI sequences). Structural connectivity and functional MRI have also been studied in this context; however, the results remain inconclusive, and there is no existing consensus on specific methods and analyses (Heinzel et al., 2019). Conventional MRI such as volumetric imaging, deformation-based imaging, or cortical thickness measures is not used routinely for diagnosis of early PD as these methods show changes usually in later stages of disease pathology (Armstrong & Okun, 2020; Krajcovicova et al., 2019; Kunst et al., 2019).

Hence, a promising approach might focus on imaging α -Syn accumulation or neuroinflammation, which occurs much earlier than neurodegeneration. In 1997, α -Syn was found to be the main component of Lewy bodies, one of the pathological hallmarks of PD (Spillantini et al., 1997). Several studies reported that mitochondrial



dysfunction, oxidative stress, or neuroinflammation cause the formation of toxic oligomeric species of α -Syn or vice versa, which may lead to degeneration of neurons (DeMaagd & Philip, 2015). Recent studies have also provided evidence that aggregated α -Syn can act as a prion-like protein transferring from one neuron to another and inducing α -Syn aggregation in the host cell (Li et al., 2008; Pan-Montojo et al., 2012). Detecting α -Syn pathology and neuroinflammation might represent the key for the early diagnosis of PD.

Diffusion kurtosis imaging (DKI), an extension of diffusion tensor imaging (DTI), is emerging as a new MRI imaging tool in the detection of early brain microstructural changes induced either by protein accumulation or neuroinflammation (Braeckman et al., 2019; Khairnar et al., 2015, 2016, 2017; Praet et al., 2018). DKI provides information about tissue complexity or heterogeneity by considering the diffusion of water as non-Gaussian (Jensen & Helper, 2010; Jensen et al., 2005). DKI provides both diffusivity and kurtosis metrics, one of being mean kurtosis (MK). It is a dimensionless metric, which reflects the degree of diffusion hindrance arising from tissue heterogeneity. If there is a higher hindrance to the diffusion of water, there is an increase in kurtosis values. MK was found to be sensitive and specific for both anisotropic white matter and isotropic gray matter microstructural changes in many neurodegenerative disorders like multiple sclerosis, Huntington disease, Alzheimer's disease as well as PD (Arab et al., 2018; Coutu et al., 2014; Guglielmetti et al., 2016; Jensen et al., 2005; Rudrapatna et al., 2014). However, clinical trials using DKI in PD are very scarce. Wang and colleagues proposed the utility and sensitivity of MK in the early diagnosis of PD for the first time (Wang et al., 2011). Later, the results were confirmed by Zhang and colleagues on 72 PD patients (yet diagnosed with motor symptoms). The study found a positive correlation of MK with Hoehn-Yahr and UPDRS-III (Unified Parkinson's Disease Rating Scale) staging (Zhang et al., 2015). Furthermore, DKI was found to be effective in differentiating PD and detecting microstructural changes in both subcortical (basal ganglia) and cortical regions and in the white matter (Ito et al., 2015; Kamagata et al., 2017; Minsterova et al., 2020; Surova et al., 2018; Zhang et al., 2015). Despite these promising results, there are still no studies aiming to identify PD-related alterations in the high-risk population at the pre-motor stage. This issue required downwards translation to animal models, where we are able to identify the underlying pathological processes responsible for the changes in the kurtosis signal. Therefore, our group initiated a large project focused on the utility of MK in detecting α -Syn accumulation-induced microstructural changes in transgenic mouse model of PD overexpressing α -Syn (TNWT-61). We observed that MK was able to capture the α -Syn accumulation (or α -Syn accumulation-induced changes) in striatum and thalamus in the very early stage of PD-like pathology in very young TNWT-61 mice (Khairnar et al., 2017) and continue providing the same result (higher MK) at later time-points in the same model (Khairnar et al., 2015, 2017).

In the present study, we aimed to deepen our knowledge on the utility and sensitivity of DKI in detecting the α -Syn-induced microstructural changes in the early stages of the diseases using the

intra-gastric rotenone (ROT) mouse model of PD. The model is based on Braak's staging of the disease in which the α -Syn pathology is first found in the gut and the dorsal motor nucleus of the vagus (DMV) and progresses to the midbrain through the dorsal motor nucleus of vagus (Braak et al., 2003). To achieve this objective, we analyzed changes in the brain of a validated ROT model (Pan-Montojo et al., 2010) after different ROT exposure times to capture and track PD-like pathology in the DMV and later in the striatum, substantia nigra, and other brain regions (Study 1). Furthermore, we wanted to assess whether oral exposure to ROT for short periods of time could lead, even in the absence of the pesticide, to similar PD-like alterations with time. Hence, we expose the mice to oral ROT only for the time known to induce the first pathological changes in the DMV but not in basal ganglia (i.e., 2 months) and we checked for PD-like pathology even after stopping ROT administration for 4 more months (Study 2).

2 | MATERIAL AND METHODS

2.1 | Animals

Male mice of the C57BL/6 strain were purchased from Charles River (Germany) at the age of 2 months and kept in the experimental animal facility of the Masaryk University (Brno, Czech Republic). The mice were group-housed in standard rodent polycarbonate cages ($n = 10$) per cage. At the age of 1 year, the animals were arbitrarily assigned to the ROT-treated and control groups treated by saline as a vehicle (VEH).

The experimental groups were exposed to VEH/ROT (5 days a week) in two experiments as follows and as depicted in Figure 1:

Study 1:

- time point 2 months (2 months followed by behavioral studies, MRI assessment, sacrifice, and sample harvest), VEH: $n = 8$, ROT: $n = 7$ mice;
- time point 3 months (exposure to ROT for 3 months followed by behavioral studies, MRI assessment, sacrifice, and sample harvest), VEH: $n = 8$, ROT: $n = 9$ mice;
- time point 4 months (exposure to ROT for 4 months followed by behavioral studies, MRI assessment, sacrifice, and sample harvest), VEH: $n = 8$, ROT: $n = 7$ mice.

Study 2:

- time point 6 months (exposure to ROT for 2 months long followed by 4 months of wash-out period, behavioral studies, MRI assessment, sacrifice, and sample harvest), VEH: $n = 8$, ROT: $n = 9$ mice.

Environmental conditions during the whole study were constant: relative humidity 50%–60%, room temperature $23^{\circ}\text{C} \pm 1^{\circ}\text{C}$, regular 12-hr light-dark cycle (6 a.m. to 6 p.m. darkness). Food and water were available ad libitum. All procedures were performed following EU Directive no. 2010/63/EU and approved by the Animal

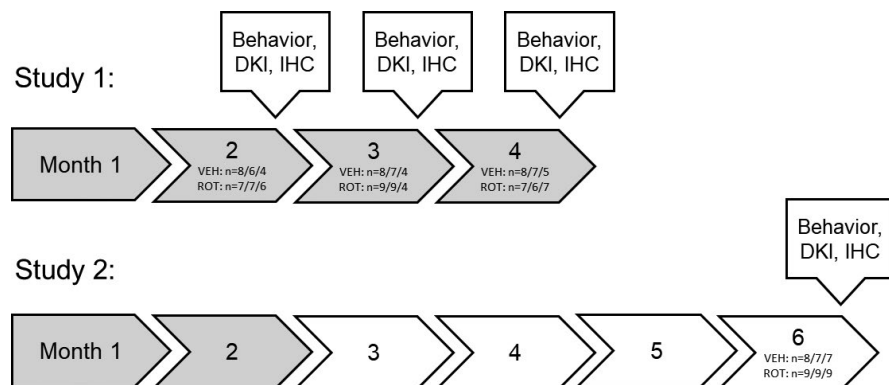


FIGURE 1 Timeline of the experiments. The schematic shows the timeline of both studies. Shaded boxes represent the time of rotenone administration (all 4 months in Study 1, month 1, and 2 in Study 2). The numbers of subjects show: *n*, number of mice included in the behavioral/DKI/IHC analyses; DKI, diffusion kurtosis imaging; IHC, immunohistochemistry, ROT, rotenone; VEH, vehicle

Care Committee of the Faculty of Medicine, Masaryk University, Czech Republic and Czech Governmental Animal Care Committee, in compliance with Czech Animal Protection Act No. 246/1992. The number of approval was MSMT-42554/2015-6. The study was not pre-registered.

2.2 | Drugs and treatments

ROT was obtained from Sigma-Aldrich spol. s.r.o., and dissolved in chloroform (50 mg in 1 ml). This solution was kept at -20°C and used to prepare the final solutions for administration during the study. The final ROT solution was prepared fresh every third day before the administration as follows. One hundred microliters of the stored ROT solution (containing 5 mg of ROT) was added to 8 ml of 2% carboxymethylcellulose solution to get 0.625 mg/ml of ROT solution. Oral gavage was used to administer 0.01 ml/g of animal weight of ROT solution. Carboxymethylcellulose solution 2% with 1.25% chloroform was used as a VEH in control animals (Pan-Montojo et al., 2010). The ROT model was generated as previously described (Pan-Montojo et al., 2010, 2012) by administration via intragastric gavage 5 days/week for 2, 3, or 4 months in the Study 1. In the case of Study 2, animals were treated only for 2 months in the same manner and used for the behavioral, MRI, and immunohistochemical study 6 months after initiation of ROT treatment.

2.3 | Behavioral profile

Behavioral tests were performed in morning hours and the order of performing behavioral studies is open field (OF) test, challenging beam walk test, square and round beam walk test, Grid Test, RotaRod test, and lastly Barnes maze test for each time point.

2.3.1 | OF test

In a brightly lit room, mice were individually tested for locomotor in OF using the Actitrack system (Panlab) as previously described

(Ruda-Kucerova et al., 2017; Ruda-Kucerova, Amchova, et al., 2018; Ruda-Kucerova, Pistovcakova, et al., 2018). Each Plexiglas arena ($45 \times 45 \times 30$ cm) was surrounded by two frames equipped with photocells located one above another at 2 and 7 cm over the cage floor. Animals were placed individually in the center of the arena. The spontaneous horizontal (distance traveled in cm) and vertical (rearing behavior, the number of episodes) locomotor activity were tracked automatically for 20 min. At the end of the session, animals were returned to their home cage, and the arenas were cleaned to remove potential olfactory cues.

2.3.2 | Challenging beam traversal test

Motor performance was measured with a challenging beam traversal test (Fleming et al., 2004, 2006; Schintu et al., 2009). Briefly, the mice were trained to traverse a 1-m non-reflective gray hardened polyvinyl chloride (PVC) beam consisting of four sections (25 cm each) with different widths (3.5–0.5 cm by 1-cm decrements) leading to the mice's home cage. After a day of training, a mesh grid (1-cm squares) of the corresponding width was placed over the beam surface, leaving approximately a 1-cm space between the grid and the beam surface. The mice were then videotaped while traversing the grid-surfaced beam for a total of three trials. Videotapes were manually scored in slow motion for the number of slips and the time to traverse across three trials by an experienced investigator blind to the experimental group. Scores were calculated across all three trials and averaged for each mouse.

2.3.3 | Square and round beam walk tests (SBW, RBW)

The beam walk tests were set up as previously described (Suidan et al., 2013). The mice traversed two 1-m long beams raised approximately 50 cm above the surface: the first beam was 10 mm wide and square, the second beam was 16 mm wide and round. To motivate the mice to cross the beam, the home cage was placed at the end of the beam. Each mouse was placed on the far end of the beam and



allowed to cross to the home cage once. The time required to cross the beam and the number of slips were counted by the person who was blind to the treatment.

2.3.4 | Grid test

The inverted grid test was used to assess neuromuscular abnormalities (Kim et al., 2010). Mice were placed in the center of a horizontal square (12 × 12 cm) grid consisting of wire mesh (mesh loop of 0.5 cm²) surrounded by non-reflective gray hardened PVC walls. The grid was placed 20 cm above a table-top and was rotated upside down, allowing the mouse to move freely. The test was performed by inverting the grid. The latency to fall off the grid was recorded with a maximum cut-off duration of 60 s.

2.3.5 | RotaRod test

This test is performed on the RotaRod apparatus (Ugo Basile) and is used to detect motor coordination. The mice were trained for three consecutive trials in a gap of 30 min one day before the test at a speed of 4 RPM for a maximum period of 300 s. At the time of testing, the animals were placed on the rod with gradually increasing the speed of RotaRod from 4 to 40 RPM in 5 min. The maximum cut-off time to stay on the rod was 5 min. After that time, the animals were moved back to their home cage. The animals received three trials with an interval of 30 min for each session. The time to fall from the rod was calculated as latency to fall in seconds.

2.3.6 | Barnes maze test

This test is used to detect spatial memory and cognition in rodents (Rosenfeld & Ferguson, 2014; Sunyer et al., 2007). Barnes maze consists of a circular arena with 20 equally distributed holes on its periphery, with one hole serving as a target zone equipped with a small shelter cage. The animal can use proximal or distal visual cues and external cues to locate and remember the target zone. Time to reach the target zone and errors in selecting the target hole was recorded to get information about the learning and memory performance.

Mice received three training trials at an interval of 15 min before the test for learning starts. For the first training trial, the mouse was placed in the center, and after exploration of two holes, they were gently guided to the target hole and left in it for 90 s. The second and third training trial procedures were the same, but mice were guided to the target hole only if necessary. Mice were given three test trials each day for five consecutive days at an interval of 15 min.

After 5 days of learning, mice received a probe trial. During the probe trial, mice were subjected to one 90-s trial identical to learning test trials except that the shelter was removed, and it appeared equal to all other 19 holes of the maze. When 90 s were over, mice were removed from the maze.

2.4 | Diffusion-weighted MR data acquisition

DKI data were obtained with a Bruker Avance 9.4T MRI system equipped with a gradient system delivering up to 660 mT/m. All experiments were performed using a quadrature volume transmit coil (inner diameter 86 mm), and a four-channel surface phased-array receive head coil. Mice were anesthetized using isoflurane inhalation (1.5%–2%) and monitored to maintain constant physiological parameters. Fast low-angle shot scout images were used to localize the bregma position. Reference T2-weighted brain scans were acquired using the 2D rapid acquisition with relaxation enhancement sequence with the following acquisition parameters: 24 × 24 mm field of view, 256 × 256 acquisition matrix size, and 15 adjacent slices of 0.5-mm slice thickness. The echo-train length for each of the echoes was set to eight, and the repetition time was 2,500 ms with four averages for a total acquisition time of ~6 min. For the DKI acquisition, diffusion-weighted images were acquired with two-shot spin-echo echo-planar imaging. Respiratory gating was used to prevent motion artifacts. The generalized autocalibrating partially parallel acquisitions with an acceleration factor of 2 was used to improve image quality by reducing sensitivity to motion and inhomogeneity of magnetic susceptibility. The DKI protocol included the acquisition of six *b* values (*b* = 0, 500, 1,000, 1,500, 2,000, and 2,500 s/mm²) along with 30 non-collinear directions for non-zero *b* values and 7 acquisitions for *b* = 0 s/mm², $\delta = 4$ ms, $\Delta = 11$ ms. The maximal *b* value of 2,500 s/mm² was proved to be the optimal setting for the WM in the DKI model, but some authors claim that this *b* value may cause an underestimation in the calculation of DKI parameters in GM (Chuhutin et al., 2017b; Hansen et al., 2017). The spin-echo echo-planar imaging pulse sequence (field of view = 24 × 24 mm, acquisition matrix = 98 × 128, echo time TE = 27 ms using 300-kHz bandwidth and repetition time ~5 s depending on the respiratory rate) was used to produce images of fifteen adjacent slices (0.5 mm thickness) within a total acquisition time of approximately 100 min. The maps in this study reflect DTI and DKI metrics: axial diffusivity (AD), radial diffusivity (RD), and mean diffusivity (MD), which reflect different diffusion directionality. AD measures the extent of diffusion occurring in the direction parallel with the fiber. RD reflects the extent of diffusion occurring in directions perpendicular to the fiber (Alexander et al., 2000, 2007), and MD is a mean value of diffusion in all directions. Kurtosis metrics: axial kurtosis (AK), radial kurtosis (RK), and MK have similar meanings, respectively.

2.4.1 | Data analysis

The acquisition matrix of DKI images was 98 × 128, which was reconstructed to 256 × 256 with the help of Paravision 5.1 software. MRI data were converted to NIfTI from the Bruker format with a Matlab script programmed locally. Diffusion data were corrected for eddy currents and motion artifacts to the first non-diffusion-weighted image (Jenkinson & Smith, 2001). The following parametric maps were calculated in ExploreDTI v4.8.4. Software (Leemans et al., 2009): MK,

AK, RK, MD, AD, RD, and fractional anisotropy (FA), using the robust estimation of tensors by outlier rejection fitting method. For further data analysis, two different approaches were applied:

ROI analysis

Averaged diffusion, FA, and kurtosis parameters were obtained from multiple regions: the DMV (average of four slices), substantia nigra (SN) (one slice), striatum (average of four slices), sensorimotor cortex (average of five slices), hippocampus (average of three slices), and thalamus (average of two slices). We chose these specific Region of interests (ROIs) based on published histology results showing a substantial accumulation of α -synuclein in these brain areas (Chesselet et al., 2012) and our previous studies with 9- and 14-month TNWT-61 mice (Khairnar et al., 2015, 2016). The ROI selection in $b = 0$ images was drawn manually according to the mouse brain atlas (Franklin & Paxinos, 2013) with the help of FA maps using ImageJ® software for various brain regions.

Tract-based spatial statistics

White matter analysis was performed using the tract-based spatial statistics (TBSS) algorithm (Smith et al., 2006) in FMRIB software library. Automatic brain extraction was carried out with brain extraction (Smith, 2002), brain-extracted maps were checked one by one visually, and the extraction was corrected manually. TBSS was implemented and modified according to the protocol for rodent brains (Sierra et al., 2011). Then, the TBSS was used with the following steps: (a) co-registration of all individual FA maps and identification of the best registration target with the free-search method; (b) application of the best registration target as a template for final transformations; (c) calculation of the mean FA map and creation of the mean FA skeleton at the threshold of 0.2 that represents the core of all tracts; (d) projection of each mouse's FA data to this skeleton; (e) repetition of the previous steps for all DKI maps. A two-sample unpaired *t* test design was set in a general linear model. A randomize tool (Winkler et al., 2014) for permutation-based non-parametric testing with 10,000 permutations, and Threshold-Free Cluster Enhancement was used for multiple comparison correction, and $p < .01$ was deemed significant (Winkler et al., 2014). The results of the TBSS analysis were identified according to the mouse brain atlas (Franklin & Paxinos, 2013).

2.4.2 | Tissue preparation for immunostaining

Mice were anesthetized after MRI acquisition intraperitoneally with Ketamine Hydrochloride (100 mg/kg, Narketan®) and Xylazine (10 mg/kg, Rometar®) and perfused transcardially with 4% paraformaldehyde in 0.1-M phosphate buffer (pH 7.4). The brain was removed and kept in 4% Paraformaldehyde for 24 hr. Tissues were transferred into 15% and then 30% sucrose, where they remained until equilibrium. Brains were then frozen using a shock-freezing technique and stored at -80°C . Brain sections (40 μm) were transferred to a 96 wells plate filled with a cryoprotectant solution containing 25%

ethylene glycol and 25% glycerin in 0.05-M phosphate and stored at -20°C until free-floating immunostaining was performed.

2.4.3 | Immunohistochemistry

Immunofluorescence was performed on 40- μm paraformaldehyde-fixed frozen sections of the brain. Brain sections were stained using a free-floating immunostaining technique. Nonspecific background staining was blocked overnight at 4°C in blocking solution (5% donkey serum [Jackson ImmunoResearch Laboratories], 0.4% Triton-X-Phosphate buffer saline [PBS]). Sections were then incubated with the primary antibody for 24 hr at 4°C , washed in PBS, incubated for one hour at RT with the fluorescent secondary antibodies, washed in PBS again, and mounted using Mowiol mounting medium. The following polyclonal primary antibodies were used: goat anti-ChAT (1:500, Catalog No. AB144P; Chemicon), sheep anti-tyrosine hydroxylase (TH) (1:1,000, Pel-Freez, Catalog No. #P60101; Rogers), rabbit anti- α -synuclein (1:400, Catalog No. sc-7011-R; Santa Cruz); chicken anti-glial fibrillary acidic protein (GFAP) (1:1,000, Catalog No. ab4674; Abcam) and rat anti-major histocompatibility complex II clone M5/114.15.2 (1:200, Catalog No. 556999; BD Pharmigen). These were coupled with the following secondary antibodies: Alexa® 555 donkey anti-rabbit (Catalog No. A-11058), anti-sheep Alexa 568 (Invitrogen, Catalog No. #A21099), Alexa® 488 anti-rabbit (Catalog No. A21206), and Alexa®594 donkey anti-sheep (Catalog No. A11016) and donkey anti-goat (Catalog No. A11058) (all 1:500 and from Invitrogen, USA, Alexa® 488 anti-rat (Catalog No. A21208; Life Technologies), donkey Rhodamine anti chicken (Catalog No. 703-296-155; Jackson ImmunoResearch).

2.4.4 | Stereological procedures

Every sixth section was stained against TH or GFAP and major histocompatibility complex II clone M5/114.15.2 and used for stereological analysis. The number of TH+ neurons in the SN or the number of GFAP+ and M5/114.15.2+ cells in the CI was estimated using the Optical Fractionator principle with StereoInvestigator software (MicroBrightField Inc.) on a Zeiss Axioplan microscope and using a 20 \times objective. Total TH+ neuron number (N) was calculated using the formula $N = \frac{1}{4} \frac{SQ}{t/h} \frac{1}{(asf)} \frac{1}{ssf}$, where $Q = \frac{1}{4}$ is the total number of cells counted, $t = \frac{1}{4}$ is the section thickness, $h = \frac{1}{4}$ is the height of optical disector, $asf = \frac{1}{4}$ is the area of sampling fraction $\frac{1}{4} \frac{a(\text{frame})}{a(x,y \text{ step})}$ and $ssf = \frac{1}{4}$ is the section sampling fraction.

2.5 | Statistical data analysis

All data were expressed as arithmetic mean \pm SD. The number of subjects per group was based on previous studies of similar design by our team (Arab et al., 2019; Khairnar et al., 2015, 2016, 2017). The



experimenters were blinded during the behavioral scoring, but no other procedures.

The effect of the PD model (ROT vs. VEH) was tested in all parameters using either an unpaired two-tailed Student's *t* test when the data passed the Kolmogorov–Smirnov normality test (most of the results) or Mann–Whitney *U* test when the data were non-parametric. No outlier test was performed. Some MRI data were excluded due to the low quality (impossible to analyze). In the immunohistochemical data, only the necessary number of subjects to reach statistical significance was used. The exact numbers appear in the timeline (Figure 1). OF test was performed over 20 min; therefore, analysis of variance (ANOVA) for repeated measures (factor: model, repeated factor: a minute of measurement) was used as appropriate. RotaRod test was analyzed in an analogous manner (factor: model, repeated factor: day of measurement). The analyses were calculated using Statistica 13.5.0.17 (Tibco Software Inc). The level of statistical significance was set at $p < .05$.

This study is an exploratory experiment using a number of ROIs and all available DKI variables to reveal the most valuable metrics. However, this approach increases the number of comparisons. Therefore, in the statistical analysis, we decided to show

non-corrected results together with CIs and accept a risk of type I error (false-positive results) to reveal potentially important differences in specific ROIs and DKI metrics similarly as in previous studies (Arab et al., 2019; Khairnar et al., 2015, 2016, 2017). The medical relevance of our data will need to be carefully tested by clinical studies in the future. Therefore, all CI and other statistical details are provided in the Tables S1–S4.

3 | RESULTS

3.1 | Study 1: time points 2–3–4 months

3.1.1 | Behavioral tests

The OF test assessed horizontal (distance traveled) and vertical (number of rearing episodes) locomotion. The data were analyzed in 1-min bins, 5-min bins, and total values. None of the analyses in any time-point rendered any significant differences between the VEH and ROT groups (only total values are shown in Table 1).

TABLE 1 Behavioral study results at 2-, 3-, and 4-month time point

	SBW time	SBW slips	RBW time	RBW slips	CBW time	CBW slips	Grid test
2 months							
VEH	6.1 ± 1.1	0.5 ± 0.5	7.8 ± 1.5	1.6 ± 1.4	20.9 ± 7.0	0.8 ± 0.5	53.7 ± 5.8
ROT	9.4 ± 2.2**	1.4 ± 1.0	9.6 ± 2.7	2.9 ± 2.7	25.5 ± 5.5	1.3 ± 0.6	49.1 ± 10.0
3 months							
VEH	8.1 ± 1.2	3.3 ± 2.3	7.1 ± 1.0	5.0 ± 3.8	10.8 ± 2.1	0.8 ± 0.2	48.4 ± 9.0
ROT	8.0 ± 1.1	1.6 ± 1.2	6.9 ± 1.5	2.4 ± 1.7	9.9 ± 1.7	1.2 ± 0.6	43.2 ± 11.1
4 months							
VEH	6.0 ± 1.3	1.6 ± 1.1	5.2 ± 0.9	1.6 ± 1.3	10.6 ± 1.4	0.6 ± 0.4	49.9 ± 9.5
ROT	6.1 ± 0.9	3.6 ± 3.0	9.4 ± 2.6**	10.4 ± 3.8***	11.7 ± 1.4	1.4 ± 0.9*	25.3 ± 7.5***
	RotaRod D1	RotaRod D2	RotaRod D3	B-maze time	B-maze errors	OF horizontal	OF vertical
2 months							
VEH	288.4 ± 16.6	294.5 ± 12.1	281.0 ± 47.8	6.7 ± 3.5	0.5 ± 0.5	3,454 ± 651	51 ± 20
ROT	272.3 ± 41.4	277.2 ± 36.2	290.2 ± 12.3	6.8 ± 1.9	1.0 ± 0.9	3,210 ± 355	38 ± 10
3 months							
VEH	264.0 ± 34.0	273.7 ± 33.6	276.5 ± 29.3	2.5 ± 2.8	2.8 ± 3.3	2,663 ± 785	34 ± 20
ROT	262.9 ± 52.4	277.3 ± 33.3	278.2 ± 33.0	8.8 ± 4.2*	1.4 ± 2.2	2,502 ± 598	44 ± 18
4 months							
VEH	247.7 ± 48.0	267.1 ± 33.7	252.9 ± 59.5	12.7 ± 4.6	2.5 ± 5.1	3,080 ± 266	43 ± 20
ROT	209.3 ± 66.5	197.3 ± 63.5	228.1 ± 52.3	4.7 ± 2.5**	1.7 ± 2.2	2,805 ± 553	28 ± 8

Note: The table summarizes the results of behavioral tests of motor performance and memory performed in time points 2–3–4 months (number of subjects was $n = 7–9$ per group). The results are mean values ± SD, results of *t* test in asterisk. Time in the beam walk tests, Barnes maze, grid test, and RotaRod is in seconds; distance in the OF is in cm; vertical episodes and slips are indicated as a number of episodes.

Abbreviations: B-maze, Barnes maze; CBW, challenging beam walk test; D1, Day 1; D2, Day 2; D3, Day 3; RBW, round beam walk; ROT, rotenone; SBW, square beam walk; VEH, vehicle.

* $p < .05$; ** $p < .01$; *** $p < .001$.



Tests of motor performance did detect a number of significant differences between the groups, particularly in the 4-month time point. Specifically, in 2 months, only time to transverse the square beam was longer in the ROT-treated mice (*t* test, $p = .004$), while no significant differences were detected in the 3-month time point. In the 4-month time-point, the ROT-treated animals exhibited a longer time to traverse the round beam (*t* test, $p = .001$) as well as a higher number of slips (*t* test, $p < .001$). A higher number of slips was observed in the challenging beam as well (*t* test, $p = .047$). The grid test findings showed a shorter time to fall from the grid in the ROT-treated mice (*t* test, $p < .001$). RotaRod test did not detect any differences between the groups at any time-point.

Barnes maze assessed spatial memory performance and detected a significant difference at the 3-month time point, where the ROT-treated mice spend more time exploring the correct hole (*t* test, $p = .011$). This is a surprising result potentially suggesting better memory retention in the ROT-treated group. However, the data are highly variable, and this result is likely a statistical artifact. As expected, an opposite finding was observed in the 4-month time point where the ROT-treated mice spend less time exploring the correct hole (*t* test, $p = .002$). All behavioral results of Study 1 are summarized in Table 1.

3.1.2 | DKI MRI in ROI

Analysis of DKI results in the ROI showed little significant results in the 2-month time point. Only MK was increased in the DMV of the ROT-treated animals (*t* test, $p = .016$). Interestingly, despite the various numbers of significant differences, their direction was equal in all ROIs and time points, i.e., kurtosis metrics were higher, and diffusivity metrics were lower.

The 3-month time point was rich in statistically significant differences in all analyzed regions. The detailed results follow.

Dorsal motor nucleus of vagus nerve: MK (*t* test, $p = .005$), AK (*t* test, $p = .024$), RK (*t* test, $p = .004$), MD (*t* test, $p = .002$), AD (*t* test, $p = .021$), and RD (*t* test, $p = .003$).

SN: MK (*t* test, $p < .001$), AK (*t* test, $p = .007$), RK (*t* test, $p = .040$), MD (*t* test, $p < .001$), AD (*t* test, $p = .006$), and RD (*t* test, $p = .006$).

Hippocampus: MK (*t* test, $p < .001$), AK (*t* test, $p = .002$), RK (*t* test, $p < .001$), MD (*t* test, $p = .011$), AD (*t* test, $p = .047$), and RD (*t* test, $p = .008$).

Sensorimotor cortex: MK (*t* test, $p < .001$), AK (*t* test, $p = .003$), and RK (*t* test, $p < .001$).

Thalamus: MK (*t* test, $p = .001$), AK (*t* test, $p = .005$), RK (*t* test, $p = .009$), MD (*t* test, $p = .002$), AD (*t* test, $p = .004$), and RD (*t* test, $p = .012$). Striatum: MK (*t* test, $p < .001$), AK (*t* test, $p = .009$), RK (*t* test, $p < .001$), MD (*t* test, $p = .005$), and RD (*t* test, $p = .007$). FA did not render any significant results in this time point.

In the 4-month time point, only three ROIs were found to be affected by the ROT treatment. Specifically, hippocampus: AK (*t* test, $p = .011$) and AD (*t* test, $p = .006$), and sensorimotor cortex: FA (*t* test, $p = .039$).

The ROI results of Study 1 are summarized in Table 2.

3.1.3 | TBSS DKI MRI

The TBSS analysis did not reveal any significant results in 2- and 4-month time points. However, in the 3-month time point, there were numerous significant differences in the ROT-treated animals.

There was a significant increase in DKI metrics (MK and AK) and decreased DTI metrics (MD, RD, AD) observed in the ROT group. No changes in FA were detected. Quality control revealed extreme outlying values in white matter in RK maps of five animals (3 VEH and 2 ROT). This may lead to false significant results. In order to avoid reporting false results, RK was omitted from TBSS.

MK (*t* test, $p < .01$) was observed to be increased unilaterally in external capsule, internal capsule, cingulum, corpus callosum, ventral spinocerebellar tract, mammillothalamic tract, nigrostriatal tract, medial longitudinal fasciculus, facial nerve, dorsal fornix, primary and secondary visual cortex, primary and secondary auditory cortex, piriform cortex, temporal association cortex, mesencephalic reticular formation, amygdalohippocampal area, anterior and posterior hypothalamic area, SN (compact part), subcoreuleus nucleus (ventral part), median Raphe nucleus, and middle and superior cerebellar peduncle.

AK (*t* test, $p < .01$) was increased bilaterally in mammillothalamic tract, mammillotegmental tract, nigrostriatal tract, medial lemniscus, medial longitudinal fasciculus, median and paramedian Raphe nucleus, fasciculus retroflexus and superior cerebellar peduncle, and unilaterally in external capsule, internal capsule, cingulum, ventral spinocerebellar tract, facial nerve, deep white layers of the superior colliculus, piriform cortex, mesencephalic reticular formation, posterior hypothalamic area, SN (compact and reticular part), subcoreuleus nucleus (ventral part), cerebral peduncle, and middle cerebellar peduncle.

MD (*t* test, $p < .01$) was found to be decreased bilaterally in external capsule, cingulum, corpus callosum, commissure of inferior colliculus, deep and intermediate white layers of the superior colliculus, mammillothalamic tract, mammillotegmental tract, nigrostriatal tract, medial longitudinal fasciculus, facial nerve, mesencephalic reticular formation, subcoreuleus nucleus (ventral part), median and paramedian Raphe nucleus, middle and superior cerebellar peduncle, and unilaterally in internal capsule, reticular nucleus, medial lemniscus, ventral spinocerebellar tract, fasciculus retroflexus, retrosplenial dysgranular cortex, amygdalohippocampal area, posterior hypothalamic area, SN (compact part), and cerebral peduncle.

AD (*t* test, $p < .01$) was decreased bilaterally in deep and intermediate white layers of the superior colliculus, mammillothalamic tract, mammillotegmental tract, nigrostriatal tract, medial longitudinal fasciculus, mesencephalic reticular formation, posterior hypothalamic area, median and paramedian Raphe nucleus, and superior cerebellar peduncle, and unilaterally in external capsule, internal capsule, reticular nucleus, piriform cortex, SN (compact part), and cerebral peduncle.

RD (*t* test, $p < .01$) was decreased bilaterally in the external capsule, cingulum, corpus callosum, central commissure of the interior

TABLE 2 DKI ROI study results at 2-, 3-, and 4-month time point in different regions

	MK	AK	RK	MD	AD	RD	FA
Dorsal nucleus of vagus nerve							
2 months							
VEH	1.220 ± 0.036	0.972 ± 0.050	1.484 ± 0.108	0.0020 ± 0.0002	0.0028 ± 0.0002	0.0016 ± 0.0002	0.358 ± 0.034
ROT	1.400 ± 0.138*	1.067 ± 0.154	1.713 ± 0.317	0.0017 ± 0.0003	0.0024 ± 0.0004	0.0013 ± 0.0003	0.393 ± 0.052
3 months							
VEH	1.227 ± 0.045	0.945 ± 0.039	1.424 ± 0.057	0.0020 ± 0.0001	0.0028 ± 0.0001	0.0016 ± 0.0001	0.335 ± 0.052
ROT	1.302 ± 0.040**	0.994 ± 0.034*	1.520 ± 0.046**	0.0019 ± 0.0001**	0.0026 ± 0.0001*	0.0015 ± 0.0001**	0.349 ± 0.022
4 months							
VEH	1.275 ± 0.040	0.944 ± 0.039	1.506 ± 0.051	0.0019 ± 0.0001	0.0027 ± 0.0002	0.0015 ± 0.0001	0.396 ± 0.036
ROT	1.245 ± 0.052	0.942 ± 0.025	1.440 ± 0.079	0.0019 ± 0.0001	0.0027 ± 0.0001	0.0015 ± 0.0001	0.377 ± 0.021
Substantia nigra							
2 months							
VEH	1.287 ± 0.103	0.844 ± 0.105	1.656 ± 0.107	0.0020 ± 0.0002	0.0033 ± 0.0005	0.0013 ± 0.0001	0.507 ± 0.057
ROT	1.363 ± 0.166	0.949 ± 0.144	1.752 ± 0.374	0.0018 ± 0.0003	0.0028 ± 0.0005	0.0013 ± 0.0002	0.468 ± 0.028
3 months							
VEH	1.179 ± 0.040	0.786 ± 0.031	1.515 ± 0.082	0.0022 ± 0.0000	0.0035 ± 0.0002	0.0015 ± 0.0000	0.497 ± 0.029
ROT	1.274 ± 0.031***	0.853 ± 0.041**	1.596 ± 0.044*	0.0020 ± 0.0001***	0.0031 ± 0.0001**	0.0014 ± 0.0001**	0.480 ± 0.033
4 months							
VEH	1.239 ± 0.076	0.829 ± 0.072	1.570 ± 0.090	0.0020 ± 0.0002	0.0034 ± 0.0005	0.0014 ± 0.0001	0.478 ± 0.037
ROT	1.253 ± 0.027	0.847 ± 0.026	1.673 ± 0.209	0.0020 ± 0.0001	0.0032 ± 0.0001	0.0014 ± 0.0001	0.472 ± 0.038
Hippocampus							
2 months							
VEH	1.204 ± 0.066	1.014 ± 0.058	1.343 ± 0.072	0.0020 ± 0.0001	0.0025 ± 0.0002	0.0017 ± 0.0001	0.252 ± 0.010
ROT	1.253 ± 0.204	1.040 ± 0.167	1.401 ± 0.235	0.0019 ± 0.0003	0.0025 ± 0.0004	0.0017 ± 0.0003	0.266 ± 0.023
3 months							
VEH	1.136 ± 0.017	0.955 ± 0.021	1.261 ± 0.021	0.0021 ± 0.0001	0.0026 ± 0.0001	0.0018 ± 0.0001	0.254 ± 0.014
ROT	1.198 ± 0.026***	1.003 ± 0.023**	1.334 ± 0.023***	0.0020 ± 0.0001*	0.0025 ± 0.0001*	0.0017 ± 0.0001**	0.259 ± 0.018
4 months							
VEH	1.118 ± 0.040	0.931 ± 0.028	1.246 ± 0.040	0.0021 ± 0.0001	0.0028 ± 0.0001	0.0018 ± 0.0001	0.286 ± 0.030
ROT	1.143 ± 0.016	0.976 ± 0.019*	1.262 ± 0.031	0.0020 ± 0.0000	0.0025 ± 0.0001**	0.0017 ± 0.0001	0.264 ± 0.008
Sensorimotor cortex							
2 months							

(Continues)



TABLE 2 (Continued)

	MK	AK	RK	MD	AD	RD	FA
VEH	1.220 ± 0.094	1.131 ± 0.106	1.305 ± 0.105	0.0019 ± 0.0002	0.0022 ± 0.0002	0.0017 ± 0.0002	0.179 ± 0.018
ROT	1.233 ± 0.168	1.112 ± 0.143	1.313 ± 0.187	0.0019 ± 0.0003	0.0022 ± 0.0003	0.0017 ± 0.0003	0.175 ± 0.019
3 months							
VEH	1.143 ± 0.034	1.034 ± 0.034	1.216 ± 0.034	0.0020 ± 0.0001	0.0023 ± 0.0001	0.0018 ± 0.0001	0.168 ± 0.008
ROT	1.203 ± 0.017***	1.084 ± 0.015**	1.283 ± 0.020***	0.0019 ± 0.0000	0.0022 ± 0.0001	0.0017 ± 0.0000	0.169 ± 0.010
4 months							
VEH	1.145 ± 0.027	1.032 ± 0.028	1.232 ± 0.040	0.0019 ± 0.0001	0.0023 ± 0.0001	0.0017 ± 0.0001	0.194 ± 0.026
ROT	1.158 ± 0.027	1.049 ± 0.024	1.224 ± 0.031	0.0019 ± 0.0001	0.0022 ± 0.0001	0.0018 ± 0.0001	0.166 ± 0.008*
Thalamus							
2 months							
VEH	1.289 ± 0.101	1.032 ± 0.088	1.463 ± 0.110	0.0018 ± 0.0002	0.0025 ± 0.0002	0.0015 ± 0.0002	0.311 ± 0.023
ROT	1.375 ± 0.242	1.083 ± 0.176	1.582 ± 0.297	0.0017 ± 0.0003	0.0023 ± 0.0004	0.0014 ± 0.0003	0.330 ± 0.037
3 months							
VEH	1.195 ± 0.026	0.940 ± 0.009	1.373 ± 0.056	0.0020 ± 0.0000	0.0027 ± 0.0001	0.0016 ± 0.0001	0.318 ± 0.039
ROT	1.274 ± 0.040**	1.001 ± 0.041**	1.459 ± 0.046**	0.0019 ± 0.0001**	0.0025 ± 0.0001**	0.0015 ± 0.0001*	0.335 ± 0.030
4 months							
VEH	1.182 ± 0.077	0.935 ± 0.059	1.350 ± 0.080	0.0020 ± 0.0002	0.0027 ± 0.0002	0.0017 ± 0.0001	0.339 ± 0.025
ROT	1.268 ± 0.092	0.966 ± 0.020	1.390 ± 0.046	0.0019 ± 0.0001	0.0026 ± 0.0001	0.0016 ± 0.0000	0.334 ± 0.018
Striatum							
2 months							
VEH							
ROT							
3 months							
VEH	1.195 ± 0.028	1.013 ± 0.028	1.335 ± 0.036	0.0019 ± 0.0001	0.0024 ± 0.0001	0.0017 ± 0.0001	0.240 ± 0.020
ROT	1.273 ± 0.031**	1.064 ± 0.030**	1.428 ± 0.040**	0.0018 ± 0.0001**	0.0022 ± 0.0002	0.0015 ± 0.0001*	0.248 ± 0.028
4 months							
VEH	1.191 ± 0.009	1.003 ± 0.017	1.332 ± 0.010	0.0019 ± 0.0000	0.0024 ± 0.0001	0.0016 ± 0.0001	0.262 ± 0.041
ROT	1.177 ± 0.021	0.979 ± 0.025	1.333 ± 0.010	0.0019 ± 0.0001	0.0025 ± 0.0001	0.0016 ± 0.0001	0.280 ± 0.029

Note: The table summarizes the results of DKI performed in time points 2–3–4 months (number of subjects was $n = 6-9$ per group). The results are mean values ± SD, results of t test in asterisks (* $p < .05$; ** $p < .01$; *** $p < .001$). Kurtosis and fractional anisotropy are dimensionless units; diffusivity values are given in mm^2/s .

Abbreviations: AD, axial diffusivity; AK, axial kurtosis; FA, fractional anisotropy; MD, mean diffusivity; MK, mean kurtosis; RD, radial diffusivity; RK, radial kurtosis; ROT, rotenone; VEH, vehicle.



colliculus, dorsal and external cortex of the inferior colliculus, intermediate and deep white layers of the inferior colliculus, perirhinal cortex, retrosplenial granular, and dysgranular cortex. The TBSS results of Study 1 are depicted in Figure 2.

3.1.4 | Immunohistochemistry

In the 2-month time point, the immunohistochemical staining was performed for GFAP in the SN and capsula interna and M5 in the SN. The M5 positive cell count was zero in all samples, but one (from the ROT-treated group) and its statistical analysis were impossible. The count of GFAP positive cells did not show any difference between the VEH and ROT groups in either brain region. While in our previously reported studies and present study, we found a significant increase in α -Syn accumulation in choline acetyltransferase positive cells in the DMV (Figure 5a).

In the 3-month time point, the immunohistochemical staining was performed for TH in the SN showing a significant decrease of TH positive cells in the ROT-treated animals (*t* test, $p = .015$) (Figure 3 and 5b).

In the 4-month time point, the immunohistochemical staining was performed for GFAP, M5, and TH in the SN and GFAP in the

capsula interna. The M5-positive cell count was zero in all samples, but three (one from the VEH- and two from the ROT-treated group) and its statistical analysis were not possible. The count of GFAP positive cells did not show any difference between the VEH and ROT groups in either brain region. The analysis of TH-positive cells in the SN showed a significant decrease in the ROT-treated animals (*t* test, $p = .004$). The results are summarized in Figure 3.

3.2 | Study 2: time point 6 months

3.2.1 | Behavioral tests

In this study, only tests of motor performance were performed. In this motor test, significant differences were observed in the square beam walk test in terms of both times to traverse (*t* test, $p < .001$) and the number of slips (*t* test, $p = .035$), where the ROT-treated animals showed a slightly better performance. This finding is unlikely to be meaningful, and we can conclude that beam walk tests are unable to sensitively detect potential motor impairment in this ROT protocol. Also, the mean number of slips was very low 1.3 in control animals and 0.4 in ROT mice. On the other hand, the grid test showed a shorter time to fall from the grid in the ROT-treated mice (*t* test, $p < .001$). The grid test was found

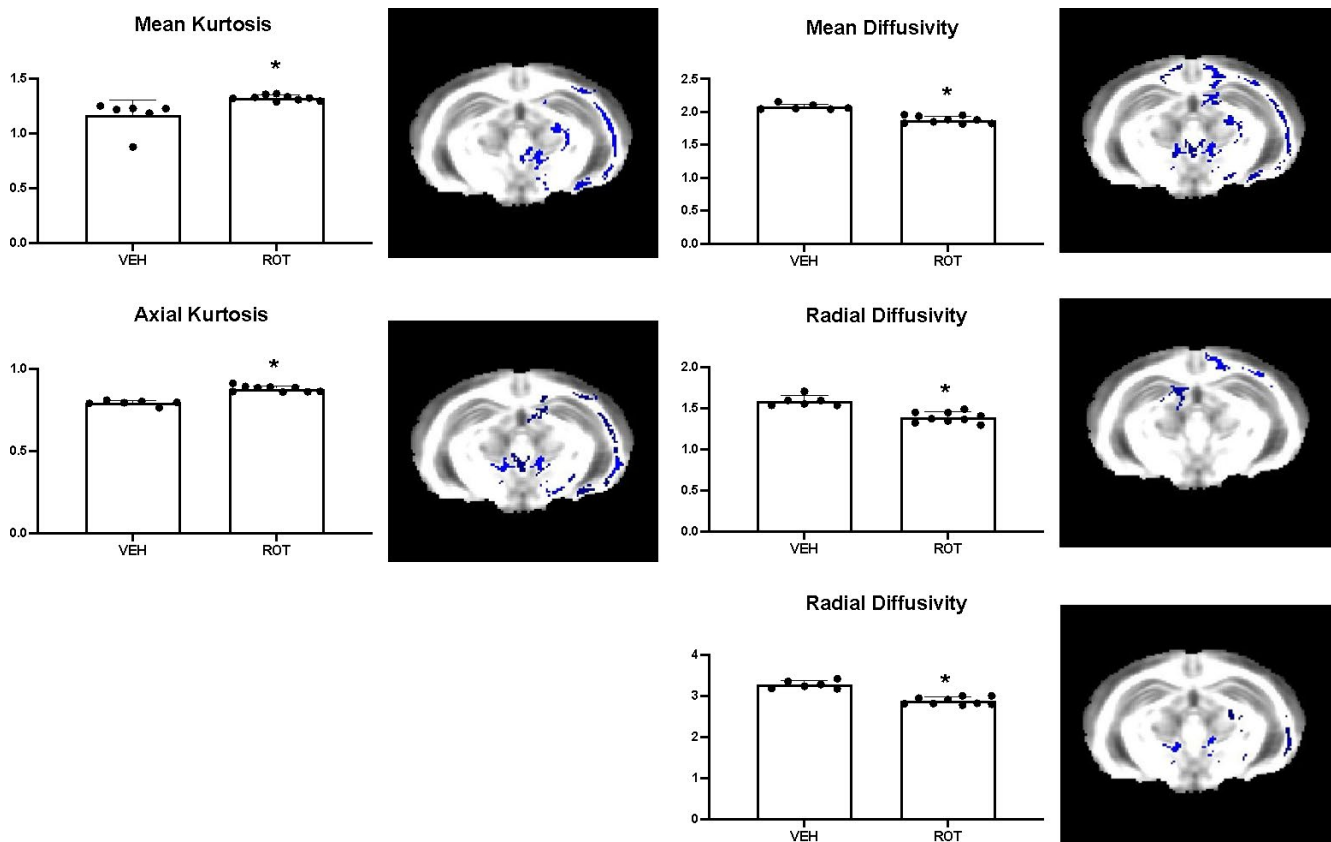


FIGURE 2 Tract-based spatial statistics (TBSS) results at 3-month time point (Study 1). Bar graphs represent averaged TBSS parameters under the altered regions; bregma position is -2.54 mm. Data are expressed as mean values \pm SD. Kurtosis is a dimensionless variable; diffusivity (MD/RD/AD) unit is 10^{-3} mm²/s. All presented changes are significant with $p < .01$ on corrected data. The numbers of animals were $n = 6$ in the VEH group and $n = 9$ in the ROT group. ROT, rotenone; VEH, vehicle

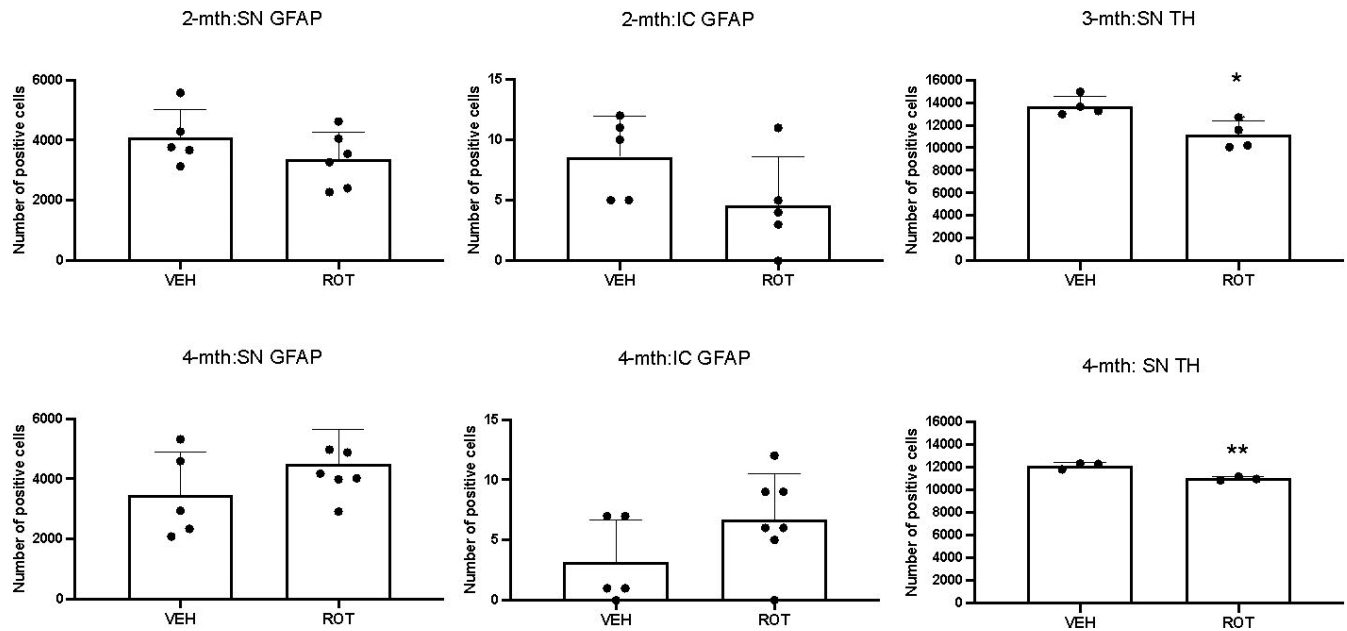


FIGURE 3 Immunohistochemical staining results in Study 1. The figure shows the results of immunohistochemical staining in time points 2–3–4 months. The results are mean values \pm SD, results of *t* test: **p* < .05, ***p* < .01, results of MWU test: #*p* < .05. The number of samples (*n*) for the glial fibrillary acidic protein positive cell count was *n* = 5 SAL and *n* = 6–7 ROT, the number of samples for the tyrosine hydroxylase positive cell count was *n* = 4 per group. IC, internal capsule; ROT, rotenone; SN, substantia nigra; VEH, vehicle

TABLE 3 Behavioral study results at 6-month time point

	SBW time	SBW slips	RBW time	RBW slips	CBW time
VEH	7.8 \pm 1.3	1.3 \pm 0.8	7.6 \pm 1.9	4.1 \pm 2.6	13.3 \pm 1.8
ROT	5.2 \pm 0.9***	0.4 \pm 0.5*	6.1 \pm 1.2	2.2 \pm 0.6	12.1 \pm 1.8
	CBW slips	Grid test	RotaRod D1	RotaRod D2	RotaRod D3
VEH	1.0 \pm 0.4	45.0 \pm 7.2	222.1 \pm 32.7	240.4 \pm 47.9	252.5 \pm 46.0
ROT	0.6 \pm 0.5	29.5 \pm 7.1***	223.7 \pm 45.6	220.9 \pm 25.4	234.4 \pm 31.3

Note: The table summarizes the results of behavioral tests of motor and memory performance in time point 6 months (number of subjects was VEH: *n* = 8, ROT: *n* = 9). The results are mean values \pm SD, results of *t* test in asterisk (**p* < .05; ****p* < .001).

Abbreviations: CBW, challenging beam walk test; D1, Day 1; D2, Day 2; D3, Day 3; RBW, round beam walk; ROT, rotenone; SBW, square beam walk; VEH, vehicle.

to be very sensitive in all of our behavioral studies (Arab et al., 2018; Khairnar et al., 2015, 2016, 2017). All behavioral results are summarized in Table 3.

3.2.2 | DKI MRI in ROI

In this study, only SN and thalamus were found to be affected by the ROT treatment. The direction of kurtosis and diffusivity differences was equal as in Study 1, i.e., kurtosis metrics were higher, and diffusivity metrics were lower.

SN: MK (*t* test, *p* = .005), RK (*t* test, *p* = .003), RD (*t* test, *p* = .004), and FA (*t* test, *p* = .001).

Thalamus: MK (*t* test, *p* < .001), AK (*t* test, *p* = .006), RK (*t* test, *p* = .002), MD (*t* test, *p* = .004), AD (*t* test, *p* = .041), and RD (*t* test, *p* = .007).

The results are summarized in Table 4.

3.2.3 | TBSS MRI

The TBSS analysis did not render any significant results at this time point.

3.2.4 | Immunohistochemistry

In the 6-month time point, the immunohistochemical staining was performed for GFAP, M5, and TH in the SN and GFAP in the capsula interna. The count of GFAP positive cells showed a significant difference between the VEH and ROT groups in capsula interna (*t* test, *p* = .006). The analysis of TH positive cells in the SN show significant differences between the VEH and ROT groups in the SN (*t* test, *p* = .023). However, the analysis of M5 in the SN did not show difference between the groups (*t* test, *p* = .0240). Despite the count of GFAP positive cells in SN did not reach statistical significance, there was a



TABLE 4 DKI ROI study results at 6-month time point in different regions

	MK	AK	RK	MD	AD	RD	FA
Dorsal nucleus of vagus nerve							
VEH	1.203 ± 0.076	0.910 ± 0.059	1.402 ± 0.098	0.0020 ± 0.0002	0.0029 ± 0.0003	0.0016 ± 0.0001	0.371 ± 0.021
ROT	1.253 ± 0.028	0.955 ± 0.024	1.461 ± 0.044	0.0020 ± 0.0001	0.0027 ± 0.0001	0.0016 ± 0.0001	0.353 ± 0.030
Substantia nigra							
VEH	1.203 ± 0.040	0.824 ± 0.018	1.498 ± 0.057	0.0021 ± 0.0001	0.0033 ± 0.0001	0.0015 ± 0.0001	0.454 ± 0.017
ROT	1.260 ± 0.022**	0.819 ± 0.031	1.618 ± 0.066**	0.0020 ± 0.0001	0.0033 ± 0.0002	0.0014 ± 0.0001**	0.505 ± 0.029**
Hippocampus							
VEH	1.121 ± 0.029	0.939 ± 0.026	1.248 ± 0.032	0.0021 ± 0.0001	0.0027 ± 0.0001	0.0018 ± 0.0001	0.269 ± 0.019
ROT	1.132 ± 0.016	0.949 ± 0.016	1.265 ± 0.022	0.0021 ± 0.0001	0.0027 ± 0.0001	0.0018 ± 0.0001	0.264 ± 0.012
Sensorimotor cortex							
VEH	1.155 ± 0.033	1.049 ± 0.036	1.231 ± 0.034	0.0019 ± 0.0001	0.0022 ± 0.0001	0.0018 ± 0.0001	0.173 ± 0.012
ROT	1.138 ± 0.018	1.025 ± 0.018	1.216 ± 0.022	0.0020 ± 0.0001	0.0023 ± 0.0002	0.0018 ± 0.0001	0.166 ± 0.039
Thalamus							
VEH	1.174 ± 0.023	0.929 ± 0.022	1.321 ± 0.035	0.0020 ± 0.0000	0.0027 ± 0.0001	0.0017 ± 0.0000	0.315 ± 0.015
ROT	1.225 ± 0.021***	0.967 ± 0.021**	1.398 ± 0.038**	0.0019 ± 0.0001**	0.0026 ± 0.0001*	0.0016 ± 0.0001**	0.327 ± 0.028
Striatum							
VEH	1.194 ± 0.035	1.005 ± 0.028	1.339 ± 0.041	0.0019 ± 0.0001	0.0024 ± 0.0001	0.0016 ± 0.0001	0.246 ± 0.023
ROT	1.196 ± 0.030	1.008 ± 0.035	1.346 ± 0.036	0.0019 ± 0.0001	0.0024 ± 0.0001	0.0017 ± 0.0001	0.239 ± 0.021

Note: The table summarizes the results of DKI performed in time point 6 months (number of subjects was VEH: n = 7, ROT: n = 9). The results are mean values ± SD, results of t test in asterisk (*p < .05; **p < .01; ***p < .001). Kurtosis and fractional anisotropy are dimensionless units; diffusivity values are given in mm²/s.

Abbreviations: AD, axial diffusivity; AK, axial kurtosis; FA, fractional anisotropy; MD, mean diffusivity; MK, mean kurtosis; RD, radial diffusivity; RK, radial kurtosis; ROT, rotenone; VEH, vehicle.

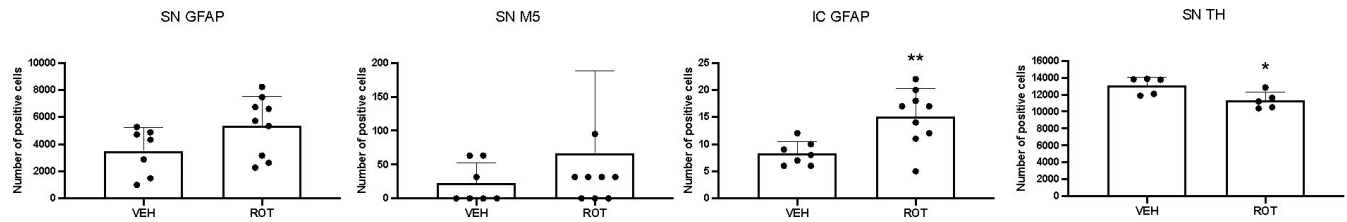


FIGURE 4 Immunohistochemical staining results in Study 2. The figure shows the results of immunohistochemical staining in time points 6 months (number of subjects was VEH: $n = 7$, ROT: $n = 9$). The results are mean values \pm SD, results of t test: * $p < .05$; ** $p < .01$. IC, internal capsule; ROT, rotenone; SN, substantia nigra; VEH, vehicle

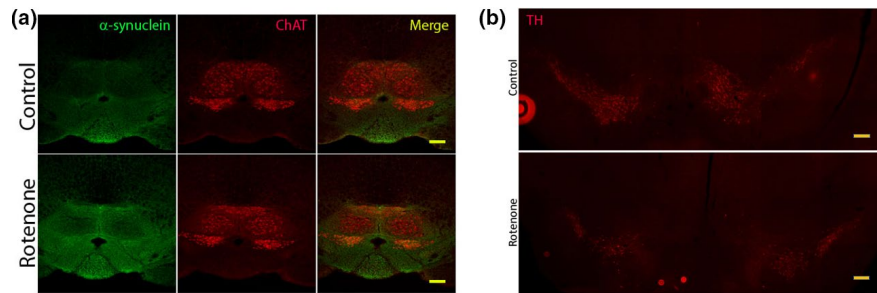


FIGURE 5 Immunohistochemical staining representative image. Figure 5a shows alpha synuclein accumulation in the choline acetyltransferase positive neurons in dorsal motor nucleus of vagus in vehicle and rotenone group (scale bar 1 micrometer is 0.66 pixel). Figure 5b shows tyrosine hydroxylase positive neurons in substantia nigra pars compacta in control and 3 months rotenone treated mice (scale bar 0.645 pixel per micrometer)

certain trend to increase in ROT mice (t test, $p = .088$). The results are summarized in Figure 4.

4 | DISCUSSION

The current study investigated the potential utility of DKI to detect the very early microstructural changes in the intragastric ROT mouse model of PD. We aimed to track the pathological changes induced by a validated protocol of the ROT model (Pan-Montojo et al., 2010, 2012) in Study 1, as well as to extend the current knowledge of the ROT-induced pathology by using only the initial part of the protocol and assessing the brain microstructure later in time (Study 2). The ROT mouse model is based on Braak's pathological staging, which claims that the α -Syn-induced pathology starts in the enteric nervous system and later progresses to SN through DMV (Braak et al., 2003; Pan-Montojo et al., 2010, 2012).

In Study 1, after 2 months of ROT administration which is similar to Braak's Stage 1, ROI-based analysis showed a significant increase in MK only in the DMV. To the best of our knowledge, this is the first study to report MK changes in DMV already in the pre-motor stage. Importantly, no other brain regions showed any differences between groups, corroborating the previous findings (Guan et al., 2019; Wang et al., 2011; Zhang et al., 2015) that MK can sensitively detect very subtle changes and might have the potential of translation as a diagnostic tool for early diagnosis of PD or identification of high-risk subjects. An increase in MK is likely to reflect the

increase in hindrance to diffusion of water molecules due to protein accumulation, neuroinflammation, or other pathology (Braeckman et al., 2019; Guglielmetti et al., 2016; Khairnar et al., 2017). A previous study in this mouse model of PD has clearly shown a significant increase in α -Syn accumulation and glial cell activation in DMV at this time point (Pan-Montojo et al., 2012). Therefore, MK seems to have the capability to identify the α -Syn accumulation or α -Syn accumulation-induced changes in the brain. This finding goes in line with our research using TNWT-61 transgenic mice overexpressing α -Syn, in which we found an increase in MK gradually spreading across brain regions with the age of the mice (Khairnar et al., 2015, 2016, 2017). Behavioral studies for motor impairment did not show any changes except square beam walk time compared to VEH-treated mice supporting the α -Syn pathology did not reach the midbrain. In accordance, we did not observe α -Syn accumulation or MK changes in the SN at 2 months.

After 3 months of ROT administration, both DKI and DTI derived metrics showed changes. These were more widespread rather than specific to one brain region, and we may conclude that the pathology had progressed from DMV to SN, representing approximately Braak's Stage 3 (Braak et al., 2003). Previous studies with an intragastric ROT mouse model found an increase in α -Syn accumulation in the SN at 3 months. In line with this, we found a significant increase in kurtosis and a decrease in diffusivity metrics representing higher structural complexity likely due to α -Syn accumulation (Pan-Montojo et al., 2010, 2012). Notably, clinical studies in PD patients also found a significant increase in MK in SN (Surova



et al., 2018; Wang et al., 2011; Zhang et al., 2017). Conversely, a very recent DKI study in both early-stage and advanced-stage PD patients reported a bilateral reduction in MK values in SN, which might be related to a decrease in structural complexity due to neuronal loss as well as the presence of iron (Guan et al., 2019). Besides the intrinsic limitations of animal models in reflecting the human pathology, the discrepancy in kurtosis results between our results and the findings of Guan et al., (2019) might be explained by the stage of the pathology, which was probably more advanced compared to our PD model (Guan et al., 2019). As we observed 15%–17% of dopaminergic neuronal loss in SN at this time point, we did not observe a significant motor impairment. Surprisingly, we did not find any changes with FA in any region, which is found to be sensitive for the diagnosis of PD patients in several clinical studies (Cochrane & Ebmeier, 2013; Vaillancourt et al., 2009). This again strengthens the role of kurtosis in the diagnosis of early stages of PD and PD-like pathology (Cochrane & Ebmeier, 2013; Langley et al., 2016; Loane et al., 2016; Vaillancourt et al., 2009; Zhang et al., 2015). Besides SN, we found significant kurtosis and diffusivity changes in DMV, striatum, thalamus, hippocampus, and sensorimotor cortex after 3 months of ROT treatment.

Interestingly, after 4 months of ROT exposure, which is similar to Braak's Stages 4 and 5, we observed significant motor impairment and decreased dopaminergic neurons count in SN, and we lost kurtosis changes in almost all ROIs except the hippocampus. The increase in kurtosis in the hippocampus goes in line with clinical studies in which PD patients show cognitive impairment after motor symptoms (Yang et al., 2016) and Braak's staging, in which PD patients show memory impairment after motor impairment (Braak et al., 2003). The significant memory impairment supports this in ROT-treated mice present after 4 months of ROT treatment.

The explanation of no changes in kurtosis might be related to the presence of more pathological processes occurring simultaneously; specifically, the kurtosis signal arising from α -Syn accumulation may be overcome by the presence of dopaminergic neuronal degeneration. α -Syn accumulation generally increases diffusional heterogeneity and ultimately increases kurtosis, whereas neurodegeneration is related to a decrease in diffusion heterogeneity, leading to a decrease in kurtosis (Arab et al., 2018; Guan et al., 2019). There is a large body of indirect evidence suggesting that at the early stage of neurodegenerative processes like AD and PD, the kurtosis values increase due to pathological protein accumulation and glial cell activation, while once the neurodegeneration occurs, it is represented by a decrease in kurtosis values (Khairnar et al., 2015, 2016, 2017; Praet et al., 2018; Vanhoutte et al., 2013). Specifically, in APP/PS1 mice, a transgenic model expressing a chimeric mouse/human amyloid precursor protein was observed an increase in kurtosis values due to amyloid-beta accumulation in the motor cortex at 8 months of age (Praet et al., 2018), while in 16-month-old APP/PS1 mice, no such findings were reported (Vanhoutte et al., 2013). This situation closely resembles results of this study using an intragastric ROT mouse model, where at 2 months, we did not find any changes in SN as there was no α -Syn pathology, at 3 months,

we observed an increase in kurtosis in many ROIs due to the presence of α -Syn, and after 4 months of ROT treatment, there was decrease in diffusional heterogeneity due to dopaminergic neurodegeneration, which nullified the kurtosis effect due to α -Syn accumulation. However, from our results of this cross-sectional study of DKI imaging in intragastric ROT-treated mice, we can conclude that MK is sensitive for detection of both early as well as late microstructural changes in PD-like pathology. Results from our recent cross-sectional human DKI study in PD patients with various phenotypes (with and without cognitive impairment and gross cortical brain atrophy) are in accord with the current findings thus further supporting the utility of DKI measures as a translational biomarker. In that study, increases of DKI parameters were present in cortical and subcortical brain regions engaged in the motor basal ganglia circuitry in the PD motor subtype with no cognitive deterioration or brain atrophy as compared to age-matched healthy controls, whereas in the more malignant subtype with mild cognitive impairment (MCI) and frontal lobe atrophy, the DKI measures were not significantly different from those in healthy age-matched controls (HC) (Minsterova et al., 2020).

TBSS, mainly used to study white matter changes, revealed similar changes as the ROI analysis. Specifically, the increase in kurtosis and decrease in diffusivity as observed in the gray matter after 3 months of ROT treatment. Conversely, it failed to detect any changes at 2 months, strengthening the evidence that α -Syn accumulation-induced changes start in gray matter and later spread to white matter. Hence, kurtosis seems to be sensitive for detecting the microstructural changes in the white matter too. Though the TBSS analysis showed significant changes at 3 months of ROT treatment only, we found an increase in kurtosis and decreased diffusivity in cingulum, corpus callosum, and medial longitudinal fasciculus, external and internal capsule, and nigrostriatal tract. These results align with our previous TBSS findings from TNWT-61 mice, in which we observed higher kurtosis in similar regions.

Furthermore, a clinical study performed by Kamagata et al., (2014) also reported changes in MK in similar regions evidencing the role of these regions in the development of PD. However, the study also found opposite results, i.e., decrease in MK and FA in corpus callosum, cingulum, and inferior longitudinal fasciculus (Kamagata et al., 2014). Of note, Sejnoha-Minsterova et al., (2020) reported decreases in MK and FA and increases in MD throughout the whole white matter skeleton only in patients with the malignant PD subtype with MCI and brain atrophy, while no differences were observed in the motor subtype as compared to HC (34). Unfortunately, we do not know much about white matter changes in our intragastric ROT mouse model. Therefore, we performed the immunofluorescence studies for GFAP in internal capsule but did not find any significant changes compared to the VEH.

In Study 2, we aimed to validate the extent of development of ROT-induced pathological process after 2 months of exposure and 4 months of wash-out. As we observed in Study 1, the pathology is developed in DMV after 2 months without apparent spreading to

SN. So far, the ROT-induced pathology was believed to be induced by ongoing chronic ROT dosing. However, this is not the case of sporadic PD, which is believed to be only triggered by pesticide exposure and seems to require a long time to develop without ongoing contact with the toxin. Hence, we based our innovative ROT model on this situation. When these animals were subjected to behavioral assessments and DKI imaging, we found a moderate (compared with 4 months of ROT exposure) motor impairment and higher MK in SN and thalamus and higher FA in the SN. This pattern resembles the 3-month time point, i.e., the zenith of the DKI signal changes observed in Study 1. The results of the Study 2 go in line with the clinical trial of Wang et al., (2011), reporting higher MK and FA in SN of PD patients as well as with the recent results of Sejnoha-Minsterova et al. showing increases particularly of MK in gray matter regions engaged in the motor basal ganglia circuitry in PD patients with a motor subtype (29,34). The pathological process responsible for increasing MK and FA might be due to α -Syn accumulation or glial cell activation as proposed by (Giannelli et al., 2012; Khairnar et al., 2016, 2017). We did perform the glial cell activation using GFAP and dopaminergic neurodegeneration using TH in SN by immunofluorescence studies. We found a significant decrease in TH positive neurons in the ROT-treated mice compared to control animals suggesting that the new ROT paradigm may be a suitable tool for the investigation of subtle pathological PD-like features, which will be most likely age dependent. It would be very interesting to track the DKI signal changes further in time.

In conclusion, the present study has two important findings: (a) MK has sensitively detected the α -Syn accumulation-induced microstructural changes already at the very prodromal stage of PD-like pathology in DMV and consistently reflected the spreading of the pathological process to other brain regions in the later stage. (b) Even after a minimal exposure to ROT (2 months), which is known to induce α -Syn pathology only in DMV but not in SN, and a long wash-out period (4 months), the α -Syn pathology reached SN and thalamus as detected by MK. Hence, the present study further supports the diagnostic utility of MK in detecting very early changes induced by α -Syn accumulation in the pre-motor stages of PD. Although the current animal model results cannot be directly compared to a human DKI cross-sectional study in various PD subtypes, the direction of DKI changes seems to be similar in presymptomatic and early symptomatic stages of the ROT-induced PD and human PD with solely motor subtype. DKI findings in a more malignant PD subtype with MCI and cross brain atrophy resemble those in the ROT model reaching the Braak's Stages 4 and 5 with more pronounced brain degeneration. This means that DKI may become the first translational biomarker that has the potential for identifying α -Syn-related brain microstructural changes already in the prodromal and early motor stages of PD and track the disease progression as well as identify malignant disease subtypes with major brain degeneration. This would make DKI a suitable biomarker for future PD studies. DKI studies are warranted in prodromal PD subjects with a longitudinal study design to confirm this assumption.

ACKNOWLEDGMENTS

The behavioral apparatuses for the Barnes maze, challenging beam traversal, and grid tests were kindly provided by Jiri Kucera, Environmental Measuring Systems, Brno, Czech Republic.

CONFLICT OF INTEREST

The authors have no conflicts of interest to declare. Experiments were conducted in compliance with the ARRIVE guidelines.

AUTHOR CONTRIBUTIONS

AK and JR designed the experiment, performed and analyzed experiments, prepared figures, and wrote the manuscript; AA performed the behavioral studies for motor and non-motor impairment; CH, QS, and AC performed the immunohistochemical studies and stereological counting; AM and NS performed the tract based spatial statistical analysis; ED and ZS performed MRI imaging of brains; FPM designed the experiments together with AK and JR, supervised its execution, performed data analysis and contributed to editing and finalizing the manuscript; IR contributed in experimental design, supervised its execution and edited and finalized the manuscript.

DATA AVAILABILITY STATEMENT

The data that support the findings of this study are available from the corresponding author upon reasonable request.

ORCID

Amit Khairnar  <https://orcid.org/0000-0003-3375-774X>
 Jana Ruda-Kucerova  <https://orcid.org/0000-0002-1846-0799>
 Eva Drazanova  <https://orcid.org/0000-0003-1844-4489>
 Irena Rektorova  <https://orcid.org/0000-0002-5455-4573>

REFERENCES

- Alexander, A. L., Hasan, K., Kindlmann, G., Parker, D. L., & Tsuruda, J. S. (2000). A geometric analysis of diffusion tensor measurements of the human brain. *Magnetic Resonance in Medicine: An Official Journal of the International Society for Magnetic Resonance in Medicine*, 44, 283–291. [https://doi.org/10.1002/1522-2594\(200008\)44:2<283::AID-MRM16>3.0.CO;2-V](https://doi.org/10.1002/1522-2594(200008)44:2<283::AID-MRM16>3.0.CO;2-V)
- Alexander, A. L., Lee, J. E., Lazar, M., & Field, A. S. (2007). Diffusion tensor imaging of the brain. *Neurotherapeutics: the Journal of the American Society for Experimental NeuroTherapeutics*, 4, 316–329. <https://doi.org/10.1016/j.nurt.2007.05.011>
- Arab, A., Ruda-Kucerova, J., Minsterova, A., Drazanova, E., Szabó, N., Starcuk, Z., Rektorova, I., & Khairnar, A. (2019). Diffusion kurtosis imaging detects microstructural changes in a methamphetamine-induced mouse model of Parkinson's disease. *Neurotoxicity Research*, 36, 724–735. <https://doi.org/10.1007/s12640-019-00068-0>
- Arab, A., Wojna-Pelczar, A., Khairnar, A., Szabó, N., & Ruda-Kucerova, J. (2018). Principles of diffusion kurtosis imaging and its role in early diagnosis of neurodegenerative disorders. *Brain Research Bulletin*, 139, 91–98. <https://doi.org/10.1016/j.brainresbull.2018.01.015>
- Armstrong, M. J., & Okun, M. S. (2020). Diagnosis and treatment of Parkinson disease: A review. *JAMA*, 323, 548–560. <https://doi.org/10.1001/jama.2019.22360>
- Braak, H., Del Tredici, K., Rüb, U., De Vos, R. A., Steur, E. N. J., & Braak, E. (2003). Staging of brain pathology related to sporadic Parkinson's



- disease. *Neurobiology of Aging*, 24, 197–211. [https://doi.org/10.1016/S0197-4580\(02\)00065-9](https://doi.org/10.1016/S0197-4580(02)00065-9)
- Braeckman, K., Descamps, B., Pieters, L., Vral, A., Caeyenberghs, K., & Vanhove, C. (2019). Dynamic changes in hippocampal diffusion and kurtosis metrics following experimental mTBI correlate with glial reactivity. *NeuroImage: Clinical*, 2s1, 101669. <https://doi.org/10.1016/j.nicl.2019.101669>
- Chesselet, M.-F., Richter, F., Zhu, C., Magen, I., Watson, M. B., & Subramaniam, S. R. (2012). A progressive mouse model of Parkinson's disease: The Thy1-aSyn ("Line 61") mice. *Neurotherapeutics: the Journal of the American Society for Experimental NeuroTherapeutics*, 9, 297–314. <https://doi.org/10.1007/s13311-012-0104-2>
- Chuhutin, A., Hansen, B., & Jespersen, S. N. (2017b). Precision and accuracy of diffusion kurtosis estimation and the influence of b-value selection. *NMR in Biomedicine*, 30, e3777. <https://doi.org/10.1002/nbm.3777>
- Cochrane, C. J., & Ebmeier, K. P. (2013). Diffusion tensor imaging in parkinsonian syndromes: A systematic review and meta-analysis. *Neurology*, 80, 857–864. <https://doi.org/10.1212/WNL.0b013e318284070c>
- Coutu, J.-P., Chen, J. J., Rosas, H. D., & Salat, D. H. (2014). Non-Gaussian water diffusion in aging white matter. *Neurobiology of Aging*, 35, 1412–1421. <https://doi.org/10.1016/j.neurobiolaging.2013.12.001>
- DeMaagd, G., & Philip, A. (2015). Parkinson's disease and its management: Part 1: Disease entity, risk factors, pathophysiology, clinical presentation, and diagnosis. *Pharmacy and Therapeutics*, 40, 504.
- Fleming, S. M., Salcedo, J., Fernagut, P.-O., Rockenstein, E., Masliah, E., Levine, M. S., & Chesselet, M.-F. (2004). Early and progressive sensorimotor anomalies in mice overexpressing wild-type human α -synuclein. *Journal of Neuroscience*, 24, 9434–9440.
- Fleming, S., Salcedo, J., Hutson, C., Rockenstein, E., Masliah, E., Levine, M., & Chesselet, M.-F. (2006). Behavioral effects of dopaminergic agonists in transgenic mice overexpressing human wildtype α -synuclein. *Neuroscience*, 142, 1245–1253. <https://doi.org/10.1016/j.neuroscience.2006.07.005>
- Franklin, K. B. J., & Paxinos, G. (2013) Paxinos and Franklin's The mouse brain in stereotaxic coordinates.
- Giannelli, M., Toschi, N., Passamonti, L., Mascalchi, M., Diciotti, S., & Tessa, C. (2012). Diffusion kurtosis and diffusion-tensor MR imaging in Parkinson disease. *Radiology*, 265, 645–646. author reply 646. <https://doi.org/10.1148/radiol.12121036>
- Guan, J., Ma, X., Geng, Y., Qi, D., Shen, Y., Shen, Z., Chen, Y., Wu, E., & Wu, R. (2019). Diffusion kurtosis imaging for detection of early brain changes in Parkinson's disease. *Frontiers in Neurology*, 10, 1285. <https://doi.org/10.3389/fneur.2019.01285>
- Guglielmetti, C., Veraart, J., Roelant, E., Mai, Z., Daans, J., Van Audekerke, J., Naeyaert, M., Vanhoutte, G., Delgado y Palacios, R., Praet, J., Fieremans, E., Ponsaerts, P., Sijbers, J., Van der Linden, A., & Verhoye, M. (2016). Diffusion kurtosis imaging probes cortical alterations and white matter pathology following cuprizone induced demyelination and spontaneous remyelination. *NeuroImage*, 125, 363–377. <https://doi.org/10.1016/j.neuroimage.2015.10.052>
- Hansen, B., Khan, A. R., Shemesh, N., Lund, T. E., Sangill, R., Eskildsen, S. F., Østergaard, L., & Jespersen, S. N. (2017). White matter biomarkers from fast protocols using axially symmetric diffusion kurtosis imaging. *NMR in Biomedicine*, 30, e3741. <https://doi.org/10.1002/nbm.3741>
- Heinzel, S., Berg, D., Gasser, T., Chen, H., Yao, C., Postuma, R. B., & MDS Task Force on the Definition of Parkinson's Disease. (2019). Update of the MDS research criteria for prodromal Parkinson's disease. *Movement Disorders*, 34, 1464–1470. <https://doi.org/10.1002/mds.27802>
- Ito, K., Sasaki, M., Ohtsuka, C., Yokosawa, S., Harada, T., Uwano, I., Yamashita, F., Higuchi, S., & Terayama, Y. (2015). Differentiation among parkinsonisms using quantitative diffusion kurtosis imaging. *NeuroReport*, 26, 267–272. <https://doi.org/10.1097/WNR.0000000000000341>
- Jenkinson, M., & Smith, S. (2001). A global optimisation method for robust affine registration of brain images. *Medical Image Analysis*, 5, 143–156. [https://doi.org/10.1016/S1361-8415\(01\)00036-6](https://doi.org/10.1016/S1361-8415(01)00036-6)
- Jensen, J. H., & Helpert, J. A. (2010). MRI quantification of non-Gaussian water diffusion by kurtosis analysis. *NMR in Biomedicine*, 23, 698–710.
- Jensen, J. H., Helpert, J. A., Ramani, A., Lu, H., & Kaczynski, K. (2005). Diffusional kurtosis imaging: The quantification of non-gaussian water diffusion by means of magnetic resonance imaging. *Magnetic Resonance in Medicine: An Official Journal of the International Society for Magnetic Resonance in Medicine*, 53, 1432–1440.
- Kalia, L. V., Kalia, S. K., & Lang, A. E. (2015). Disease-modifying strategies for Parkinson's disease. *Movement Disorders*, 30, 1442–1450.
- Kamagata, K., Tomiyama, H., Hatano, T., Motoi, Y., Abe, O., Shimoji, K., Kamiya, K., Suzuki, M., Hori, M., Yoshida, M., Hattori, N., & Aoki, S. (2014). A preliminary diffusional kurtosis imaging study of Parkinson disease: Comparison with conventional diffusion tensor imaging. *Neuroradiology*, 56, 251–258. <https://doi.org/10.1007/s00234-014-1327-1>
- Kamagata, K., Zalesky, A., Hatano, T., Ueda, R., Di Biase, M. A., Okuzumi, A., Shimoji, K., Hori, M., Caeyenberghs, K., Pantelis, C., & Hattori, N. (2017). Gray matter abnormalities in idiopathic P arkinson's disease: Evaluation by diffusional kurtosis imaging and neurite orientation dispersion and density imaging. *Human Brain Mapping*, 38, 3704–3722.
- Khairnar, A., Latta, P., Drazanova, E., Ruda-Kucerova, J., Szabó, N., Arab, A., Hutter-Paier, B., Havas, D., Windisch, M., Sulcova, A., Starcuk, Z., & Rektorova, I. (2015). Diffusion kurtosis imaging detects microstructural alterations in brain of α -synuclein overexpressing transgenic mouse model of Parkinson's disease: A pilot study. *Neurotoxicity Research*, 28, 281–289. <https://doi.org/10.1007/s12640-015-9537-9>
- Khairnar, A., Ruda-Kucerova, J., Drazanova, E., Szabó, N., Latta, P., Arab, A., Hutter-Paier, B., Havas, D., Windisch, M., Sulcova, A., Starcuk, Z., Király, A., & Rektorova, I. (2016). Late-stage α -synuclein accumulation in TNWT-61 mouse model of Parkinson's disease detected by diffusion kurtosis imaging. *Journal of Neurochemistry*, 136, 1259–1269. <https://doi.org/10.1111/jnc.13500>
- Khairnar, A., Ruda-Kucerova, J., Szabó, N., Drazanova, E., Arab, A., Hutter-Paier, B., Neddens, J., Latta, P., Starcuk, Z., & Rektorova, I. (2017). Early and progressive microstructural brain changes in mice overexpressing human α -Synuclein detected by diffusion kurtosis imaging. *Brain, Behavior, and Immunity*, 61, 197–208. <https://doi.org/10.1016/j.bbi.2016.11.027>
- Kim, S. T., Son, H. J., Choi, J. H., Ji, I. J., & Hwang, O. (2010). Vertical grid test and modified horizontal grid test are sensitive methods for evaluating motor dysfunctions in the MPTP mouse model of Parkinson's disease. *Brain Research*, 1306, 176–183. <https://doi.org/10.1016/j.brainres.2009.09.103>
- Krajcovicova, L., Klobusiakova, P., & Rektorova, I. (2019). Gray matter changes in Parkinson's and Alzheimer's disease and relation to cognition. *Current Neurology and Neuroscience Reports*, 19, 1–9. <https://doi.org/10.1007/s11910-019-1006-z>
- Kunst, J., Marecek, R., Klobusiakova, P., Balazova, Z., Anderkova, L., Nemcova-Elfmakova, N., & Rektorova, I. (2019). Patterns of grey matter atrophy at different stages of Parkinson's and Alzheimer's diseases and relation to cognition. *Brain Topography*, 32, 142–160. <https://doi.org/10.1007/s10548-018-0675-2>
- Langley, J., Huddleston, D. E., Merritt, M., Chen, X., McMurray, R., Silver, M., Factor, S. A., & Hu, X. (2016). Diffusion tensor imaging of the substantia nigra in Parkinson's disease revisited. *Human Brain Mapping*, 37, 2547–2556. <https://doi.org/10.1002/hbm.23192>
- Leemans, A., Jeurissen, B., Sijbers, J., & Jones, D. K. (2009). ExploreDTI: A graphical toolbox for processing, analyzing, and visualizing diffusion



- MR data. In *17th Annual Meeting of Intl Soc Mag Reson Med*, Hawaii, USA.
- Li, J.-Y., Englund, E., Holton, J. L., Soulet, D., Hagell, P., Lees, A. J., Lashley, T., Quinn, N. P., Rehnroona, S., Björklund, A., Widner, H., Revesz, T., Lindvall, O., & Brundin, P. (2008). Lewy bodies in grafted neurons in subjects with Parkinson's disease suggest host-to-graft disease propagation. *Nature Medicine*, *14*, 501–503. <https://doi.org/10.1038/nm1746>
- Loane, C., Politis, M., Kefalopoulou, Z., Valle-Guzman, N., Paul, G., Widner, H., Foltynie, T., Barker, R. A., & Piccini, P. (2016). Aberrant nigral diffusion in Parkinson's disease: A longitudinal diffusion tensor imaging study. *Movement Disorders*, *31*, 1020–1026. <https://doi.org/10.1002/mds.26606>
- Oertel, W. H. (2017). Recent advances in treating Parkinson's disease. *F1000Research*, *6*, 260. <https://doi.org/10.12688/f1000research.10100.1>
- Pan-Montojo, F., Anichtchik, O., Dening, Y., Knells, L., Pursche, S., Jung, R., Jackson, S., Gille, G., Spillantini, M. G., Reichmann, H., & Funk, R. (2010). Progression of Parkinson's disease pathology is reproduced by intragastric administration of rotenone in mice. *PLoS One*, *5*(1), e8762. <https://doi.org/10.1371/journal.pone.0008762>
- Pan-Montojo, F., Schwarz, M., Winkler, C., Arnhold, M., O'Sullivan, G. A., Pal, A., Said, J., Marsico, G., Verbavatz, J.-M., Rodrigo-Angulo, M., Gille, G., Funk, R. H. W., & Reichmann, H. (2012). Environmental toxins trigger PD-like progression via increased alpha-synuclein release from enteric neurons in mice. *Scientific Reports*, *2*, 1–12. <https://doi.org/10.1038/srep00898>
- Postuma, R. B., Berg, D., Stern, M., Poewe, W., Olanow, C. W., Oertel, W., Obeso, J., Marek, K., Litvan, I., Lang, A. E., Halliday, G., Goetz, C. G., Gasser, T., Dubois, B., Chan, P., Bloem, B. R., Adler, C. H., & Deuschl, G. (2015). MDS clinical diagnostic criteria for Parkinson's disease. *Movement Disorders*, *30*, 1591–1601. <https://doi.org/10.1002/mds.26424>
- Praet, J., Manyakov, N. V., Muchene, L., Mai, Z., Terzopoulos, V., de Backer, S., Torremans, A. N., Guns, P.-J., Van De Castele, T., Bottelbergs, A., Van Broeck, B., Sijbers, J., Smeets, D., Shkedy, Z., Bijmens, L., Pemberton, D. J., Schmidt, M. E., Van der Linden, A., & Verhoye, M. (2018). Diffusion kurtosis imaging allows the early detection and longitudinal follow-up of amyloid- β -induced pathology. *Alzheimer's Research & Therapy*, *10*, 1–16. <https://doi.org/10.1186/s13195-017-0329-8>
- Rey, N. L., Petit, G. H., Bousset, L., Melki, R., & Brundin, P. (2013). Transfer of human α -synuclein from the olfactory bulb to interconnected brain regions in mice. *Acta Neuropathologica*, *126*, 555–573. <https://doi.org/10.1007/s00401-013-1160-3>
- Rosenfeld, C. S., & Ferguson, S. A. (2014). Barnes maze testing strategies with small and large rodent models. *Journal of Visualized Experiments*, *84*, e51194. <https://doi.org/10.3791/51194>
- Ruda-Kucerova, J., Amchova, P., Machalova, A., Pistovcakova, J., & Sulcova, A. (2018). Prenatal exposure to modafinil alters locomotor behaviour and leucocyte phagocytosis in mice. *Psychiatria Danubina*, *30*, 356–366. <https://doi.org/10.24869/psyd.2018.356>
- Ruda-Kucerova, J., Babinska, Z., Amchova, P., Stark, T., Drago, F., Sulcova, A., & Micale, V. (2017). Reactivity to addictive drugs in the methylazoxymethanol (MAM) model of schizophrenia in male and female rats. *The World Journal of Biological Psychiatry*, *18*, 129–142. <https://doi.org/10.1080/15622975.2016.1190032>
- Ruda-Kucerova, J., Pistovcakova, J., Amchova, P., Sulcova, A., & Machalova, A. (2018). Prenatal exposure to modafinil alters behavioural response to methamphetamine in adult male mice. *International Journal of Developmental Neuroscience*, *67*, 37–45. <https://doi.org/10.1016/j.ijdevneu.2018.03.005>
- Rudrapatna, S. U., Wieloch, T., Beirup, K., Ruscher, K., Mol, W., Yanev, P., Leemans, A., van der Toorn, A., & Dijkhuizen, R. M. (2014). Can diffusion kurtosis imaging improve the sensitivity and specificity of detecting microstructural alterations in brain tissue chronically after experimental stroke? Comparisons with diffusion tensor imaging and histology. *NeuroImage*, *97*, 363–373. <https://doi.org/10.1016/j.neuroimage.2014.04.013>
- Saeed, U., Compagnone, J., Aviv, R. I., Strafella, A. P., Black, S. E., Lang, A. E., & Masellis, M. (2017). Imaging biomarkers in Parkinson's disease and Parkinsonian syndromes: Current and emerging concepts. *Translational Neurodegeneration*, *6*, 1–25. <https://doi.org/10.1186/s40035-017-0076-6>
- Schintu, N., Frau, L., Ibba, M., Garau, A., Carboni, E., & Carta, A. R. (2009). Progressive dopaminergic degeneration in the chronic MPTP mouse model of Parkinson's disease. *Neurotoxicity Research*, *16*, 127–139. <https://doi.org/10.1007/s12640-009-9061-x>
- Segura-Aguilar, J., Paris, I., Muñoz, P., Ferrari, E., Zecca, L., & Zucca, F. A. (2014). Protective and toxic roles of dopamine in Parkinson's disease. *Journal of Neurochemistry*, *129*, 898–915. <https://doi.org/10.1111/jnc.12686>
- Sejnova Minsterova, A., Klobusiakova, P., Pies, A., Galaz, Z., Mekyska, J., Novakova, L., Elfmarkova, N. N., & Rektorova, I. (2020). Patterns of diffusion kurtosis changes in Parkinson's disease subtypes. *Parkinsonism & Related Disorders*, *81*, 96–102. <https://doi.org/10.1016/j.parkreldis.2020.10.032>
- Sierra, A., Laitinen, T., Lehtimäki, K., Rieppo, L., Pitkänen, A., & Gröhn, O. (2011). Diffusion tensor MRI with tract-based spatial statistics and histology reveals undiscovered lesioned areas in kainate model of epilepsy in rat. *Brain Structure and Function*, *216*, 123–135. <https://doi.org/10.1007/s00429-010-0299-0>
- Smith, S. M. (2002). Fast robust automated brain extraction. *Human Brain Mapping*, *17*, 143–155. <https://doi.org/10.1002/hbm.10062>
- Smith, S. M., Jenkinson, M., Johansen-Berg, H., Rueckert, D., Nichols, T. E., Mackay, C. E., Watkins, K. E., Ciccarelli, O., Cader, M. Z., Matthews, P. M., & Behrens, T. E. J. (2006). Tract-based spatial statistics: Voxelwise analysis of multi-subject diffusion data. *NeuroImage*, *31*, 1487–1505. <https://doi.org/10.1016/j.neuroimage.2006.02.024>
- Spillantini, M. G., Schmidt, M. L., Lee, V.-M.-Y., Trojanowski, J. Q., Jakes, R., & Goedert, M. (1997). α -Synuclein in Lewy bodies. *Nature*, *388*, 839–840. <https://doi.org/10.1038/42166>
- Suidan, G. L., Duerschmied, D., Dillon, G. M., Vanderhorst, V., Hampton, T. G., Wong, S. L., Voorhees, J. R., & Wagner, D. D. (2013). Lack of tryptophan hydroxylase-1 in mice results in gait abnormalities. *PLoS One*, *8*, e59032. <https://doi.org/10.1371/journal.pone.0059032>
- Sunyer, B., Patil, S., Höger, H., & Lubec, G. (2007). Barnes maze, a useful task to assess spatial reference memory in the mice. *Protocol Exchange*. Retrieved June 19, 2016 from <http://www.nature.com/protocolexchange/protocols/349>
- Surova, Y., Nilsson, M., Lampinen, B., Lätt, J., Hall, S., Widner, H., van Westen, D., & Hansson, O. (2018). Alteration of putaminal fractional anisotropy in Parkinson's disease: A longitudinal diffusion kurtosis imaging study. *Neuroradiology*, *60*, 247–254. <https://doi.org/10.1007/s00234-017-1971-3>
- Vaillancourt, D., Spraker, M., Prodoehl, J., Abraham, I., Corcos, D., Zhou, X., Comella, C., & Little, D. (2009). High-resolution diffusion tensor imaging in the substantia nigra of de novo Parkinson disease. *Neurology*, *72*, 1378–1384. <https://doi.org/10.1212/01.wnl.0000340982.01727.6e>
- van Rumund, A., Green, A. J., Fairfoul, G., Esselink, R. A., Bloem, B. R., & Verbeek, M. M. (2019). α -Synuclein real-time quaking-induced conversion in the cerebrospinal fluid of uncertain cases of parkinsonism. *Annals of Neurology*, *85*, 777–781. <https://doi.org/10.1002/ana.25447>
- Vanhoutte, G., Pereson, S., Delgado y Palacios, R., Guns, P.-J., Asselbergh, B., Veraart, J., Sijbers, J., Verhoye, M., Van Broeckhoven, C., & Van



- der Linden, A. (2013). Diffusion kurtosis imaging to detect amyloidosis in an APP/PS1 mouse model for Alzheimer's disease. *Magnetic Resonance in Medicine*, 69, 1115–1121. <https://doi.org/10.1002/mrm.24680>
- Wang, J.-J., Lin, W.-Y., Lu, C.-S., Weng, Y.-H., Ng, S.-H., Wang, C.-H., Liu, H.-L., Hsieh, R.-H., Wan, Y.-L., & Wai, Y.-Y. (2011). Parkinson disease: Diagnostic utility of diffusion kurtosis imaging. *Radiology*, 261, 210–217. <https://doi.org/10.1148/radiol.11102277>
- Winkler, A. M., Ridgway, G. R., Webster, M. A., Smith, S. M., & Nichols, T. E. (2014). Permutation inference for the general linear model. *NeuroImage*, 92, 381–397. <https://doi.org/10.1016/j.neuroimage.2014.01.060>
- Yang, Y., Tang, B.-S., & Guo, J.-F. (2016). Parkinson's disease and cognitive impairment. *Parkinson's Disease*, 2016, 1–8.
- Zhang, G., Zhang, C., Zhang, Y., Wang, Y., Nie, K., Zhang, B., Xie, H., Lu, J., & Wang, L. (2017). The effects of striatal silent lacunar infarction on the substantia nigra and movement disorders in Parkinson's disease: A follow-up study. *Parkinsonism & Related Disorders*, 43, 33–37. <https://doi.org/10.1016/j.parkreldis.2017.06.020>
- Zhang, G., Zhang, Y., Zhang, C., Wang, Y., Ma, G., Nie, K., Xie, H., Liu, J., & Wang, L. (2015). Diffusion kurtosis imaging of substantia nigra

is a sensitive method for early diagnosis and disease evaluation in Parkinson's disease. *Parkinson's Disease*, 2015, 1–5.

SUPPORTING INFORMATION

Additional supporting information may be found online in the Supporting Information section.

How to cite this article: Khairnar, A., Ruda-Kucerova, J., Arab, A., Hadjistyllis, C., Sejnoha Minsterova, A., Shang, Q., Chovsepain, A., Drazanova, E., Szabó, N., Starcuk, Z. Jr., Rektorova, I., & Pan-Montojo, F. (2021). Diffusion kurtosis imaging detects the time-dependent progress of pathological changes in the oral rotenone mouse model of Parkinson's disease. *Journal of Neurochemistry*, 158, 779–797. <https://doi.org/10.1111/jnc.15449>